Charles University in Prague
Faculty of Mathematics and Physics

MASTER THESIS

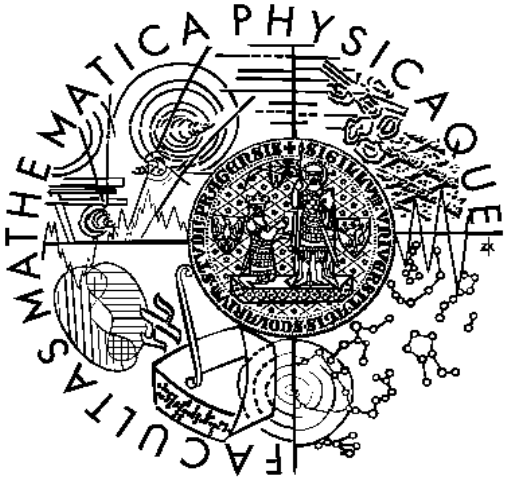

Petra Adamová

Earthquake source process and its complexity

Department of Geophysics
Supervisor: Doc. RNDr. Jiří Zahradník, DrSc.
Study program: Physics

Acknowledgements

I would like to express my vast thanks to Jiří Zahradník for his invaluable support, guidance and help with this work. Other thanks go to Efthimios Sokos for interesting discussions and several versions of his unpublished new Matlab software. Christoforos Benetatos and Roula Roumelioti helped me with data and SAC. Ladislav Hanyk and Vladimír Plicka provided another software and data advice. Seismograms from NOA stations are also to be acknowledged. Kind atmosphere for my work was created thanks to the department staff and students. Last but not at least, I am very grateful to my parents for their support and patience during my studies.

Some figures were made with Generic Mapping Tools, Wessel and Smith (1991). The work was supported by EU project 004043(GOCE)-3HAZ-CORINTH.

Prohlašuji, že jsem svou diplomovou práci napsala samostatně a výhradně s použitím citovaných pramenů. Souhlasím se zapůjčováním práce.

V Praze dne 21.4.2006 Petra Adamová

Contents

Abstract 4

1 Motivation **5**

2 Method **6**
2.1 Iterative deconvolution 6
2.2 Inversion modes 8
2.3 Steps of inversion 11

3 Long-period disturbances **14**

4 Applications **18**
4.1 Amfilochia earthquake 18
4.2 Vartholomio earthquake 33
4.3 Lefkada aftershock 48

5 Discussion and conclusion **57**

A Shortcuts **59**

References **60**

Název práce: Zdrojový proces zemětřesení a jeho složitost
Autor: Petra Adamová
Katedra: Katedra geofyziky
Vedoucí diplomové práce: Doc. RNDr. Jiří Zahradník, DrSc.
e-mail vedoucího: jz@karel.troja.mff.cuni.cz
Abstrakt: Je studována momentová inverze násobného bodového zdroje. Všechny inverze jsou počítány pomocí programového balíku ISOLA (Fortran). Tento program je zobecněním metody popsané v Kikuchi a Kanamori (1991) pro regionální data (Zahradník et al., 2005b). Hlavní těžiště práce je v testování a aplikaci této metody na tři vybrané jevy z oblasti západního Řecka: na ostrově Lefkada (14. 8. 2003), poblíž města Amfilochia (31. 12. 2002) a u města Vartholomio (2. 2. 2002). Pro dvě z těchto aplikací (Amfilochia, Vartholomio) byla seismologickými agenturami hlášena velká nesmyková (CLVD) složka. Oba tyto jevy byly v této práci vysvětleny jako násobné. Třetí jev považujeme za jednoduchý, ale řešení není uspokojivé. Při přípravě dat byla v záznamech objevena nová dlouhoperiodická porucha, v textu nazývaná 'myš druhého druhu', a provedeno její odstranění. Jsou rovněž odstraněny 'myši prvního druhu' studované dříve v článku Zahradník a Plešinger (2005a). Z práce vyplynulo několik obecných poučení, shrnutých v závěrečné kapitole.
Klíčová slova: momentová inverze, násobný model zdroje, ISOLA, 'myši'

Title: Earthquake source process and its complexity
Author: Petra Adamová
Department: Dept. of Geophysics
Supervisor: Doc. RNDr. Jiří Zahradník, DrSc.
Supervisor's e-mail address: jz@karel.troja.mff.cuni.cz
Abstract: Moment tensor inversion of multiple-point source events is studied. All inversions are computed using program package ISOLA. It is generalization of Kikuchi and Kanamori (1991) method for regional data (Zahradník et al., 2005b). The main substance of the work is in tests and application of this method on three selected events from the area of western Greece: on the island Lefkada (August 14, 2003), near the town Amfilochia (December 31, 2002) and near the town Vartholomio (December 2, 2002). High non-shear component (CLVD) was reported for two of these applications (Amfilochia and Vartholomio). Both events were interpreted in this thesis as multiple events. The third event is considered to be a single point event, but solution for that earthquake is not satisfactory. During data preparation, a new long-period disturbance was detected an removed, called in this text as 'mouse-2' type. 'Mice-1' type, studied by Zahradník and Plešinger (2005a), were also removed from records. Some general lessons emerging from this work are summarized in the last chapter.
Keywords: moment inversion, multiple point source, ISOLA, 'mice'

Chapter 1

Motivation

Earthquakes indicate a big complexity, and that is why seismologists have started detailed studies of the source process. Quick moment tensor inversion for significant earthquakes ($M > 5$) is provided by many major agencies (e.g., Harvard since 1976, USGS, MEDNET, SED). For large earthquakes, the European earthquake center EMSC (http://www.emsc-csem.org) provides all moment tensor inversions in one figure (from up to roughly 8-10 contributors).

For long time people studied only point solution because they were restricted by computer equipment and low number of high-quality broadband seismographs. Fifteen years ago, Kikuchi and Kanamori (1991), see also references in that paper, started with multiple point solutions from teleseismic data. They applied this method for events in Japan and many other regions. Their code is freely available. In this study we used a similar method for regional data (completely new code ISOLA - ISOLated Asperities) written by Zahradník (2005b) - i.e. waveform inversion from regional data based on iterative deconvolution. For some events, automatic (unconstrained) inversions produce a high non-DC component, which may be not realistic for typical tectonic earthquakes. In this work we try to explain events with high non-DC component as multiple events because two separate events with mechanism near to pure shear can together give mechanism with a high non-DC component. Our studied region (western Greece) belongs to the most seismically active part of Europe. The region is widely studied by many seismologists worldwide. A European collaborative project is focused on the Gulf of Corinth and this thesis has been partly related to it through the ISOLA package (project 3HAZ coordinated P. Bernard). Two from three earthquakes studied in this thesis were previously investigated by other authors, using different methods (Benetatos, 2004; Roumelioti, 2005).

Chapter 2

Method

2.1 Iterative deconvolution

We use the iterative deconvolution of multiple point sources based on Kikuchi and Kanamori (1991). We start from the point approximation of a single source. The displacement **u** caused by seismic moment tensor **M** is given by

$$u_i(t) = \sum_p \sum_q M_{pq} * G_{ip,q}, \tag{2.1}$$

where **G** is the Green's tensor, comma in subscript denotes spatial derivative and $*$ means the time convolution. Symmetric tensor **M** has 6 independent components. Arbitrary moment tensor **M** can be represented as linear combination of the so-called "elementary mechanisms" M^k.

$$M_{pq} = a^k M^k_{pq}. \tag{2.2}$$

These elementary mechanisms M^k_{pq} form a tensor base.

$$u_i(t) = \sum_p \sum_q \left(\sum_{k=1}^{6} a^k M^k_{pq} \right) * G_{ip,q}. \tag{2.3}$$

Choice of the tensor base is arbitrary. We use elementary mechanisms shown in Figure 2.1 and the corresponding elementary moment tensors are in equation 2.4.

Figure 2.1: 6 elementary mechanisms.

$$M^1 = \begin{pmatrix} 0 & 1 & 0 \\ 1 & 0 & 0 \\ 0 & 0 & 0 \end{pmatrix} M^2 = \begin{pmatrix} 0 & 0 & 1 \\ 0 & 0 & 0 \\ 1 & 0 & 0 \end{pmatrix} M^3 = \begin{pmatrix} 0 & 0 & 0 \\ 0 & 0 & -1 \\ 0 & -1 & 0 \end{pmatrix}$$

$$M^4 = \begin{pmatrix} -1 & 0 & 0 \\ 0 & 0 & 0 \\ 0 & 0 & 1 \end{pmatrix} M^5 = \begin{pmatrix} 0 & 0 & 0 \\ 0 & -1 & 0 \\ 0 & 0 & 1 \end{pmatrix} M^6 = \begin{pmatrix} 1 & 0 & 0 \\ 0 & 1 & 0 \\ 0 & 0 & 1 \end{pmatrix}. \tag{2.4}$$

By reordering we get

$$u_i(t) = \sum_{k=1}^{6} a^k \left(\sum_p \sum_q M_{pq}^k * G_{ip,q} \right) = \sum_{k=1}^{6} a^k E_i^k(t). \tag{2.5}$$

In this way the displacement **u** is approximated by a linear combination of "elementary seismograms" E^k. The elementary seismograms are computed by discrete wave number (Bouchon, 1981; program AXITRA), e.g. elementary seismogram for elementary mechanism 1:

$$E_i^1 = \sum_p \sum_q M_{pq}^1 \cdot G_{ip,q},$$

where

$$M^1 = \begin{pmatrix} 0 & 1 & 0 \\ 1 & 0 & 0 \\ 0 & 0 & 0 \end{pmatrix}.$$

Thus

$$E_i^1 = G_{ix,y} + G_{iy,x}.$$

Equation 2.5 represents linear relation between **a** and **u**. We solve inverse problem, i.e. assume knowledge of crustal model (represented by **G**), and pass form data (represented by observed displacements **u**) to the parameters a^k. The least-square solution of this problem is given by

$$\mathbf{a} = (E^T E)^{-1} E^T \mathbf{u}, \tag{2.6}$$

where T denotes transpose matrix and -1 stands for inverse matrix. From coefficients a^k we easily get the moment tensor using equations 2.2 and 2.4. Eigenvalues of the system matrix provide information about physical meaning of the formal solution. Problem is ill posed if one eigenvalue is much smaller than the other. To detect such a case, we always check the ratio between the minimum and maximum eigenvalue.

Once we find the solution, it is possible to evaluate the so-called residual error.

$$\Delta = \sum_j \int (u_j(t) - a_k E_{jk})^2 \, dt, \tag{2.7}$$

where we summed over stations and components. Step by step we arrive to

$$\Delta = \int u^2(t)dt - 2(E^T\vec{u})_k(E^TE)^{-1}_{km}(E^T\vec{u})_m$$
$$+(E^TE)_{km}(E^TE)^{-1}_{km}(E^T\vec{u})_m(E^TE)^{-1}_{mk}(E^T\vec{u})_k.$$

Thus

$$\Delta = \int u^2(t)dt - (E^T\vec{u})_k(E^TE)^{-1}_{km}(E^T\vec{u})_m.$$

Introducing correlation ψ,

$$\psi = \frac{(E^T\vec{u})_k(E^TE)^{-1}_{km}(E^T\vec{u})_m}{\int u^2(t)dt}.$$

also called the variance reduction

$$\psi = 1 - \frac{\Delta}{\int u^2(t)dt}, \tag{2.8}$$

we see that requirement of minimal residual error is equivalent to maximal correlation ψ. In the least square method with a fixed (assumed) source position and time, there is no means how to manipulate ψ. However, ψ can be maximized (i.e. Δ minimized) through variation of either the source position, or time shift, or both; see later.

2.2 Inversion modes

There are four possible modes of inversion:

1. Full moment tensor inversion
   All six elementary mechanisms are employed in inversion, i.e. we found coefficient $a^1, \ldots, a^6$.

2. Deviatoric moment tensor inversion
   Elementary mechanism 1 - 5 are used in inversion, i.e. a^6=0, the volumetric component is assumed to be zero. The remaining deviatoric tensor may contain a non-shear (CLVD) component.

3. Constrained double-couple moment tensor inversion
   In this case both the volumetric and non-shear (CLVD) components are requested to be zero. For this constraint we use the Lagrange multipliers.

4. Moment tensor inversion with fixed mechanism
   This is the situation when we assume knowledge of the mechanism (e.g. from some major agencies, or from a previous point solution) and we seek only time and source position.

In all applications we compute only deviatoric part (item 2) and from that we analyze only DC part of moment tensor because non-DC part is very unstable and we don't trust

determination of this part. We trust that there can be some small non-DC part but we are not able to determine it.

Now let us present derivation of case 3, absent in the paper of Kikuchi and Kanamori (1991).

We solve equation $E\mathbf{a} = \mathbf{u}$ with constraint $D(\mathbf{a}) = 0$, where E is matrix of our problem (elementary seismograms), $\mathbf{u}$ are data (displacement), $\mathbf{a}$ are coefficient to be found (coefficient a^k) and D is determinant of matrix E. We minimize equation

$$F + \lambda D = 0,$$

where $F(\mathbf{a}) = (E\mathbf{a} - \mathbf{u})^2$.

$$\frac{\partial F}{\partial \mathbf{a}} + \lambda \frac{\partial D}{\partial \mathbf{a}} = 0$$

$$E^T E\mathbf{a} - E^T\mathbf{u} + \lambda \frac{\partial D}{\partial \mathbf{a}} = 0 \tag{2.9}$$

$$\mathbf{a} = (E^T E)^{-1} E^T \mathbf{u} - (E^T E)^{-1} \frac{\partial D}{\partial \mathbf{a}} \lambda \tag{2.10}$$

This equation must be solved with constraint

$$D(\mathbf{a}) = 0. \tag{2.11}$$

Comparison of equations 2.6 and 2.10 shows that the first term on the right-hand side of equation 2.10 represents the 'unconstrained' solution. The second term is correction changing the deviatoric (unconstrained) solution into the pure-shear solution. It can be solved approximately in two ways.

a) We linearize equations 2.10 and 2.11 and solve the new linearizied system.

b) We solve numerically equations 2.10 and 2.11.

ad a)

Linearization of 2.11:

$$D(\mathbf{a}) = 0 \Leftrightarrow D^0 + \frac{\partial D}{\partial \mathbf{a}}|_{a_0} \Delta\mathbf{a} = 0,$$

where a^0 is the zeroth approximation. We must work with $\Delta\mathbf{a}$ instead of $\mathbf{a}$:

$$a_j = a_j^0 + \Delta a_j.$$

By analogy we apply increments to eq. 2.10:

$$E^T E(\mathbf{a} + \Delta\mathbf{a}) - E^T\mathbf{u} + \lambda \frac{\partial D}{\partial \mathbf{a}}|_{a^0} = 0.$$

We solve system

$$R\Delta\mathbf{a} + \lambda \frac{\partial D}{\partial \mathbf{a}}|_{a^0} = G^T\mathbf{u} - R\mathbf{a}^0 \tag{2.12}$$

$$\frac{\partial D}{\partial \mathbf{a}}|_{a^0} \Delta\mathbf{a} = -D^0,$$

where we use notation $R = E^T E$.
In components, we get

$$R_{11}\Delta a_1 + R_{12}\Delta a_2 + \ldots + R_{15}\Delta a_5 + \lambda \frac{\partial D}{\partial a_1}|_{a_1^0} = RHS1$$

$$\vdots$$

$$R_{51}\Delta a_1 + R_{52}\Delta a_2 + \ldots + R_{55}\Delta a_5 + \lambda \frac{\partial D}{\partial a_1}|_{a_5^0} = RHS5$$

$$\frac{\partial D}{\partial a}|_{a_1^0}\Delta a_1 + \ldots + \frac{\partial D}{\partial a}|_{a_5^0}\Delta a_5 + 0 = -D^0,$$

where RHS means the right-hand side of the equation 2.12. We rewrite this system in the matrix notation:

$$\begin{pmatrix} R & F^T \\ F & 0 \end{pmatrix} \begin{pmatrix} \Delta \mathbf{a} \\ \lambda \end{pmatrix} = \begin{pmatrix} RHS \\ -D^0 \end{pmatrix}$$

We denote

$$S = \begin{pmatrix} R & F^T \\ F & 0 \end{pmatrix}.$$

We find one matrix S repeatedly from $a_1^0, \ldots, a_5^0$ to a_1^1, a_1^2, etc. We again update right-hand side, determinant D and derivative $\frac{\partial D}{\partial a}|_{a^1}$, and so on for next iterations.

ad b)
We solve system

$$\mathbf{a} = R^{-1}E^T\mathbf{u} - R^{-1}\frac{\partial D}{\partial \mathbf{a}}\lambda = \mathbf{a}^{NDC} - R^{-1}\frac{\partial D}{\partial \mathbf{a}}\lambda$$

$$D(\mathbf{a}) = 0.$$

Because $D(\mathbf{a}(\lambda)) = 0$ is non-linear equation, we solve it iteratively. We start from zeroth approximation $\mathbf{a}^0$ (e.g. DC part of $\mathbf{a}^{NDC}$). We express explicitly

$$\mathbf{a}^1 = \mathbf{a}^0 - R^{-1}\frac{\partial D}{\partial \mathbf{a}}|_{a^0},$$

substitute $D(\mathbf{a}^1(\lambda)) = 0$ and solve numerically, for example, by bisection. We got new $\mathbf{a}^1$, determine $\frac{\partial D}{\partial \mathbf{a}}|_{a^1}$, compose new non-linear equations $D(\mathbf{a}(\lambda)) = 0$, and solve again. To stop the iteration proces we request a large DC percentage (DC% $> 90\%$), and, simultaneously, we request a high correlation ($> 50\%$).

2.3 Steps of inversion

This part is no more taken from literature. We always work in the following three steps, see Figure 2.2:

step 1: point source: optimization of the centroid depth (trial source positions situated below the reported epicenter)
step 2: point source: optimization of the horizontal position of the centroid C in the depth found in step 1
step 3: multiple point source: plane passing through the centroid C of step 2, and having also strike and dip found in step 2 (two options: fault plane I or II)

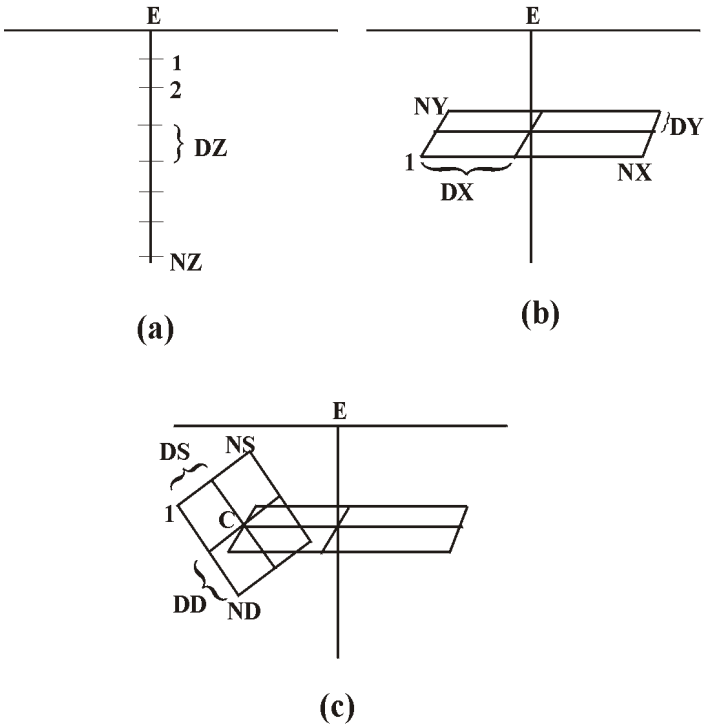

Figure 2.2: Three steps of the inversion, discussed in the text. a) step 1 - fixing epicenter (E) to found the optimum depth, b) step 2 - fixing depth to found the optimum centroid (C), c) step 3 - trial fault plane passing through C. Note the denotation of grid steps, used throughout the text.

Velocity records were instrumentally corrected, band-pass filtered, and integrated to displacement. The amplitude response of the filter is characterized by four frequencies (f1, f2, f3 and f4). It is flat between f2, f3, while two cosine tapers are applied at the two edges, between f1, f2 and f3, f4, respectively. For brevity, we denote it as, for example, 0.01-0.08-0.10-0.20 Hz. Synthetics are always filtered with exactly the same filter. For single point solution we select frequency range from the following viewpoint. Frequency

f1 and f2 we choose with respect to low-frequency noise. Frequency f3 and f4 we select so that we can represent source process with one point.

In all steps of the inversion, weights can be used. In this study we assign the weights as reciprocal peak values of the displacement time histories in the currently studied frequency range, but any other weighting can be easily used because the weights are prescribed numerically.

We work iteratively, the point source solution is called subevent. Using complete waveform data we compute the first subevent. This subevent is subtracted from the data, thus we get the so-called residual seismograms. These residual seismograms are used as new data and we retrieve the next subevent, and so on. At the end we take the final residual seismogram, subtract it from the original data, and so we get the resulting synthetic seismograms.

As described above (for a single source), for each subevent we determine its optimum time and position. To this goal, we make a grid search among the prescribed trial origin time and source positions to minimize residual error (i.e. to maximize correlation) in equation 2.8.

Variance reduction

Each subevent (after optimization) is characterized by the resulting variance reduction, given by the following formula

$$\text{varred} = 1 - \frac{|\mathbf{u} - \mathbf{s}|}{|\mathbf{u}|},$$

where $|.|$ denotes L2 norm, while $\mathbf{u}$ and $\mathbf{s}$ represent the data and synthetics, respectively. Summation in the computation of the norm is over time, stations and components. In one application (Vartholomio earthquake - see Chapter 4.2) we compute variance reduction for each station and component separately; then we sum only over time.

Crustal model

In all applications we use crustal model of Haslinger et al. (1999), see Table 2.1. The main reason for the choice is that we prefer a single model for all studied events, and this model proved to provide relatively good agreement between observed and synthetic low-frequency seismograms in some preliminary tests. Moreover, the model was derived for a region comprising one of the studied events (Amfilochia). There is no special reason to assume general applicability of the model.

Empirical relations

For estimation size of fault we use Somerville et al. (1999) empirical relations. We use only some of these relations: between the rupture area A and scalar seismic moment M_0, and between the area covered by asperities A_a and scalar seismic moment belongs to the asperities M_a:

$$A = 2.23 \cdot 10^{-15} \cdot M_0^{2/3}$$

and

$$A_a = (2.23 \cdot 10^{-15} \cdot M_a^{2/3})/2.56.$$

depth of layer top (km)	v_p (km/s)	v_s (km/s)
0.	3.5	1.9
0.5	5.47	2.7
2.0	5.5	2.86
5.0	6.0	3.23
10.0	6.2	3.24
15.0	6.48	3.40
20.0	6.7	3.80
30.0	6.75	3.81
40.0	8.0	4.66

Table 2.1: Crustal model of Haslinger et al. (1999)

Total area of asperity is 22% from the area of the whole fault. Following these relations we select spatial steps (DS, DD; see Figure 2.2) for multiple point solution.

Data from Internet

We studied one more application (earthquake near Cythera Island, January 8, 2006) but this event is not include in thesis because we did not finish it yet. Data for this quake were obtained from Internet. We downloaded them from three centers: IRIS, ORFEUS and GEOFON:
www.iris.edu/cgi-bin/wilberII_page1.pl,
http://orfeus.knmi.pl/cgi-bin/wilberII/wilberII_page1.pl,
www.gfz-potsdam.de/cgi-bin/geofon/request?mode=nform.
IRIS and ORFEUS provide their data through web interface WILBER II. This interface is a user-friendly application and provides data for moderate and large events. WILBER II at IRIS has more options for plotting map of stations, record section (i.e. records for more stations), etc. However, at IRIS there are no data from the NOA network that we need. As a rule, data are available in almost real time ($\sim$ 1-2 hours after earthquake). But for this event data from Geofon network were available only after three days and only on ORFEUS and GEOFON.

We download data in SEED or SAC (binary or ASCII) format. SAC format from IRIS and ORFEUS is not the 'whole' SAC format. It contains only waveforms, not information about the stations (in particular, not the instrumental transfer function). Therefore we prefer to download data in SEED format and convert to SAC using a UNIX program Rdseed (freely available from IRIS home page).

The GFZ Seismological Data Archive (network GEOFON) provides their data using WebDC archive - it is continuation of NetDC concept. Users have access to all data in the WebDC archive, i.e. not only to the data related to a some big earthquake. From this WebDC archive we can download data only in SEED format.

Chapter 3

Long-period disturbances

At some stations we occasionally observe long-period disturbances (long pulses). These disturbances occur at different instruments (Guralp CMG-3T, STS-2, Lennarz-3D/20). As a rule, they are related to some earthquake, but sometimes they appear even without earthquakes. Sometimes they are quite obvious (visually clearly 'seen'), sometimes not. In both cases they are very dangerous because can destroy the earthquake signal, at least in some (long-period) range. We often study earthquakes from a few regional stations only, thus it is very important to remove 'mice' from record. We distinguish between two types of disturbances. 'Mouse-1' type was studied by Zahradník and Plešinger (2005a). Type 2 is newly introduced in this thesis. Both types can be explained and modeled as instrumental response to a specific input motion.

We start from the so called 'mouse-1' type disturbance. This disturbance is caused by step in acceleration. Step in acceleration corresponds to ramp in velocity (linear variation of velocity), see Figure 3.1. Response of instrument Le-3D/20s and Guralp CMG-3T is different because these instruments have different corner frequency and spectral slope. For Le-3D/20s the spectral decay below the corner frequency is of power 3, while for Guralp CMG-3T it is of power 2. 'Mouse-1' appears only on horizontal components, and that is why it can be related to a sudden tilt. This question, however, is not solved in this thesis. We only try to remove the disturbance from the record.
Example of 'mouse 1' from M5.5 earthquake at a distance of about 100 km is in Figure 3.2.

The second disturbance, that we call 'mouse-2' type, is caused by ramp (linear function) in acceleration (step in the derivative acceleration), see Figure 3.4. Such a disturbance can be found on all three components. The origin of this disturbance is probably in electronics of the seismographs (Plešinger, 2002). It occurs during earthquake, before it, or after, sometimes even several times within 1 hour, see Figure 3.5.

We describe removing 'mice' in more detail. We explain these disturbances by forward modeling. First we describe removing 'mouse-1' type. We use poles and zeros of the transfer function and calculate displacement response, first with unit input step in acceleration, with its onset at time t=0. We work with displacement because on the Le-3D/20sec velocity records this disturbance is not seen (it is 'hidden'). Then we adjust the amplitude and onset time of the model response by visually matching the record. The fitted response is then subtracted from signal, and, finally, the signal is again differentiated to produce

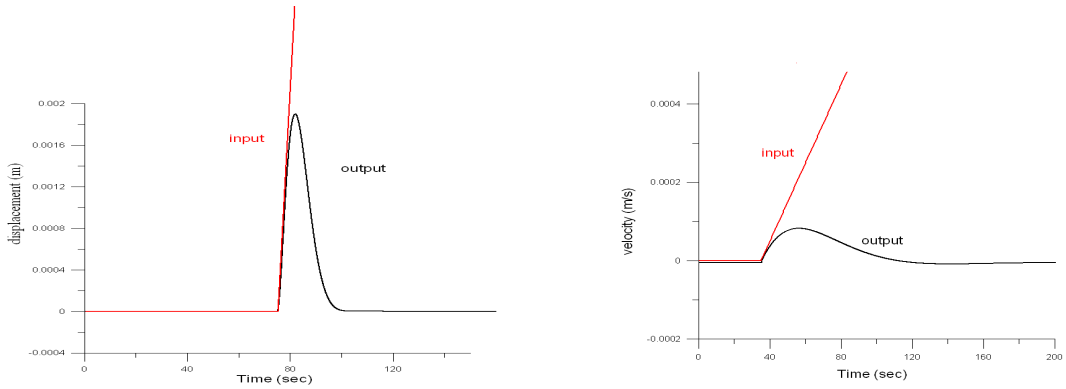

Figure 3.1: : Response of instruments to input step in acceleration. Red curves - equivalent input velocity ramp. Black curves - output of two different instruments. Left panel is displacement output for instrument Le-3D/20s and for the acceleration step of amplitude $A = 4.5 \cdot 10^{-4} m/s^2$. Right panel is velocity output for CMG3-T and the step of $A = 10^{-5} m/s^2$.

corrected velocity record. 'Mouse-2' type is modeled by analogy to 'mouse-1' type.

We analyze very carefully records from all stations for all events because 'mouse' at one station can destroy our inversion.

A few words about small disturbances, detectable, but comparable to the signal. 'Mice-2' present less problems than 'mice-1'. Fitting of 'mouse-2' is easier because this disturbance looks like a 'smooth Heaviside', so it differs from regular seismic signals very much. Moreover 'mouse-2' with small amplitude doesn't discourage the inversion. Indeed, after removing these small 'mice-2', in filtered data we see a very small difference. If we compute inversion with and without removing these small 'mice', the difference in correlation is only around 1%, for example see Figure 3.3. Anyway, in spite of their small effect we try to remove all detected disturbances of 'mice-2' type.

On the other hand, small 'mouse-1' type in signal is more problematic, because it is very badly recognizable, but filtered displacement is very different from that without 'mouse'; see Figures 4.30, 4.32 and 4.34 discussed later in chapter Applications.

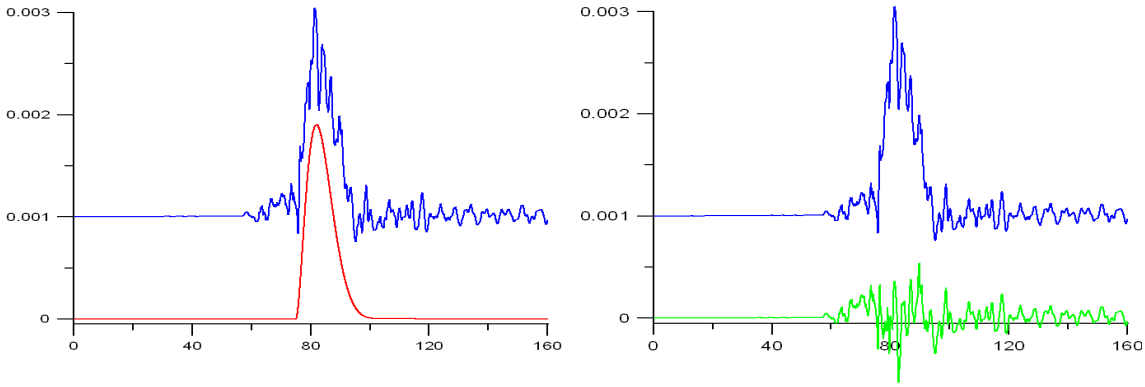

Figure 3.2: Real M5.5 earthquake (Vartholomio earthquake, studied later in this thesis), EW component at a station ITM at the epicentral distance of about 100km. 'Mouse 1' type. Left panel - blue curve: integrated velocity record in full frequency band, red curve: model response of step in acceleration. Right panel - blue curve is the same as at the left panel, green curve - data minus model response.

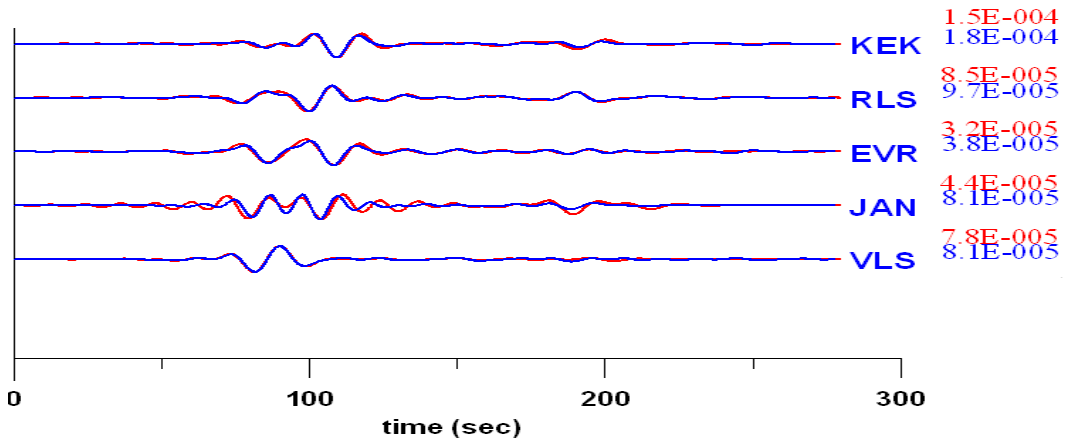

Figure 3.3: Example of 'mouse-2' type, blue curves: observed displacement with removing 'mice-2' type, red curve: observed displacement without removing these 'mice'.

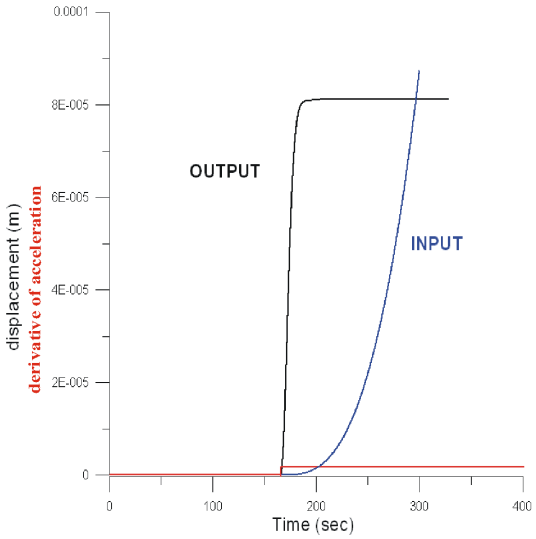

Figure 3.4: 'Mouse-2' type, red curve - step in derivative of acceleration, blue curve - input displacement, black curve - output displacement for Le3D/20s seismograph.

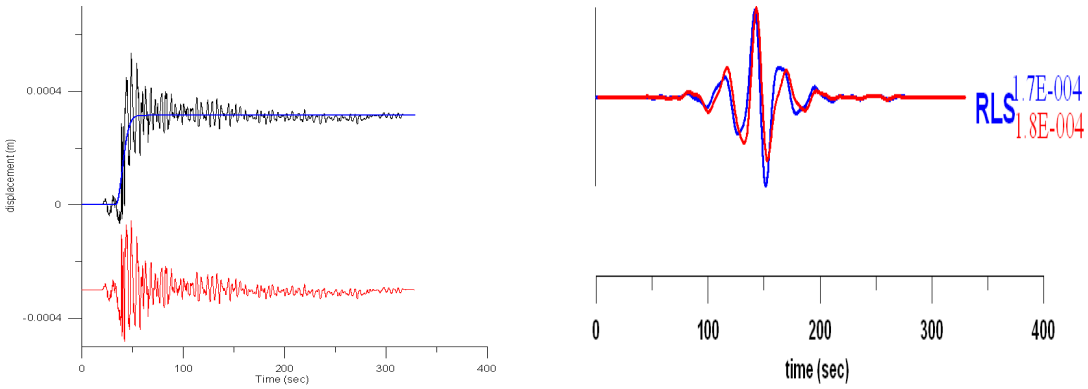

Figure 3.5: Example of 'mouse-2' type, left panel: black curve - integrated unfiltered velocity record, blue curve - model response of ramp in acceleration, red curve - data minus model response, right panel: red curve - filtered displacement without removing 'mouse-1' type, blue curve - filtered displacement after removing 'mouse-1' type, f = 0.04-0.08 Hz. (For this station difference in inversion before after removing 'mouse' was 5%.)

Chapter 4

Applications

Seismograms for this study were provided from two sources: (i) Network of Lennartz Le-3D/20s stations operated by the Institute of Geodynamics, National Observatory of Athens (NOA), and (ii) Guralp CMG 3-T stations jointly operated by the Charles University Prague and the University of Patras (P-P); see Table 4.1. For more details, see
http://www.gein.noa.gr/
http://seis30.karlov.mff.cuni.cz/ and
http://seismo.geology.upatras.gr/

station	name	agency	latitude	longitude
RLS	Riolos Achaia	NOA	38.0578	21.4667
EVR	Evritania	NOA	38.9167	21.8087
JAN	Janene	NOA	39.6567	20.8508
KEK	Kerkira	NOA	39.7130	19.7987
SER	Sergoula	P-P	38.4133	22.0566
ATH	Athina	NOA	37.9720	23.7170
ITM	Ithomi Messinia	NOA	37.1786	21.9252
KZN	Kozani	NOA	40.3070	21.7710
VLS	Valsamata Kefalonia	NOA	38.1750	20.5900

Table 4.1: Seismic stations used in this study

4.1 Amfilochia earthquake

Three moderate size events ($M_w \sim 4.5$) occurred near the town of Amfilochia, close to the Gulf of Amvrakikos, Western Greece on December 31, 2002. The source parameters, as determined by three agencies, are in Table 4.2. It is interesting that all the three events occurred within one hour, and relatively large non-shear components were reported for all of them.

Here we study the largest event of the sequence, that of $M_w(SED) = 4.96$ at 20:28 UTC. Four nearest broadband stations were selected for the waveform modeling (EVR,

		origin time (UTC)	lat.N (deg)	lon.E (deg)	depth (km)	M_0 (10^{16} Nm)	mag *)
SED	mainshock +)	20:28:33	39.00	21.25	27	3.13	4.96
	aftershock 1 +)	20:47:3	38.93	21.18	24	1.25	4.70
	aftershock 2 +)	21:22:21	38.94	21.19	27	1.39	4.73
MEDNET	mainshock +)	20:28:34.3	38.91	21.38	29	3.00	4.9
PATNET	mainshock	20:28:32.17	38.94	21.17	17.7		3.96
	aftershock 1	20:47:3.85	38.95	21.20	16.21		4.01
	aftershock 2	21:22:23.23	38.96	21.19	13.11		4.49

		strike (deg)	dip (deg)	rake (deg)	strike (deg)	dip (deg)	rake (deg)	DC%
SED	mainshock	52	48	-64	196	48	-116	30
	aftershock 1	66	51	-46	189	56	-131	32
	aftershock 2	84	70	-18	180	73	-159	35
MEDNET	mainshock	53	54	-61	189	45	-124	40

Table 4.2: Basic information about the Amfilochia earthquake from three agencies.

*) 'Mag' means magnitude, for SED and MEDNET moment magnitude and for PATNET duration magnitude.
+) origin time, latitude and longitude are for centroid

JAN, RLS and KEK), with epicentral distance ranging from 50 to 150 km, see Figure 4.1 and Table 4.3. Good signal-to-noise ratio was found for frequencies as low as 0.04 Hz.

station	distance (km)	azimuth (deg)
EVR	49.1	99.4
JAN	80.6	334.9
RLS	106.3	169.7
KEK	148.0	302.8

Table 4.3: Stations used for the Amfilochia earthquake.

A three step procedure (that of Chapter 2.3) was applied. In step 1 we made the low-frequency point source retrieval in the frequency band 0.02-0.04-0.08-0.11 Hz. Weights were applied in the inversion, using reciprocal peak values in the studied frequency band. We tested 10 trial source positions under the epicenter reported by SED. We started with coarse vertical spacing DZ = 5 km, sampling the depth range from 5 to 50 km, and then we continued with a finer spacing of 2 km (from 7 to 25 km). The optimum point source solution was found at the depth of 17 km, see Fig. 4.2. Focal mechanism obtained from this step was 88, 72, -31 (189, 61, -159) and scalar seismic moment was $M_0 = 1.06.10^{16}$ Nm.

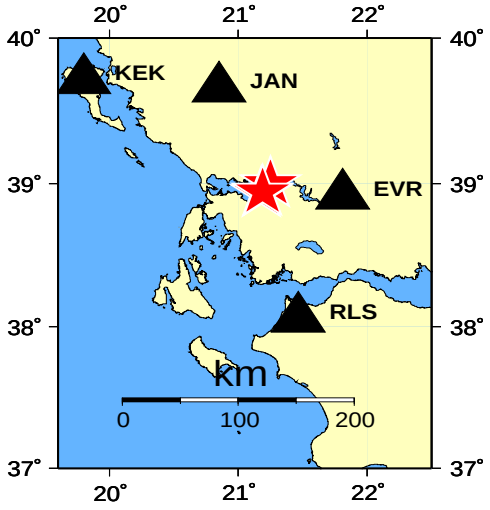

Figure 4.1: Amfilochia earthquake - red stars: location from SED: mainshock and two aftershocks, black triangles: stations used. Three stars joint in two stars.

In step 2, fixing the depth of 17 km, we tested 5 x 5 positions in a horizontal plane, first with spacing of DX = DY = 5 km, then with 2 km. From this step we got the centroid shift of 3 km to the west and 3 km to the south with respect to the SED epicenter, see Figure 4.3.

The improvement between the solution without and with the shift is 8% in the correlation (from 61% to 69%), see Fig. 4.4. An interesting observation is that the main difference between these two solutions, as regards the waveform, can be only seen on the Z component at two stations, EVR and, mainly RLS.

Focal mechanism obtained from this step 77, 72, -27 (176, 64, -160) is slightly different from that of the previous step 88, 72, -31 (181, 61, -159). The scalar seismic moment is similar to that obtained from step 1 ($M_0 = 1.15.10^{16}$ Nm). The fact that the difference is not large indicates stability. Although the difference is small, we believe that final value 77, 72, -27 (176, 64,-160) is better because it is based on the centroid source position (C) constrained by the waveform modeling.

A note should be made about the NS component at the station KEK. In the processing described above (step 1 and 2) we used all stations and components. The modeling resulted in a good agreement between the observed and synthetics waveforms, except the indicated single component at KEK. It is the component of the least amplitudes, where the effect of noise is probably not negligible (although, at first glance, it is not obvious). At NS component data are only up to 196 sec, the rest are only zeros.

To understand the influence of the KEK-NS record, we also tried to remove this component from the inversion, and repeated step 1 and step 2. The results were the same as in the previous solution. It means that the centroid position was not affected by the mentioned problem, and we can use it in the following step. Anyway, before going into more details, mainly at higher frequencies, in the all next experiments we remove KEK-NS

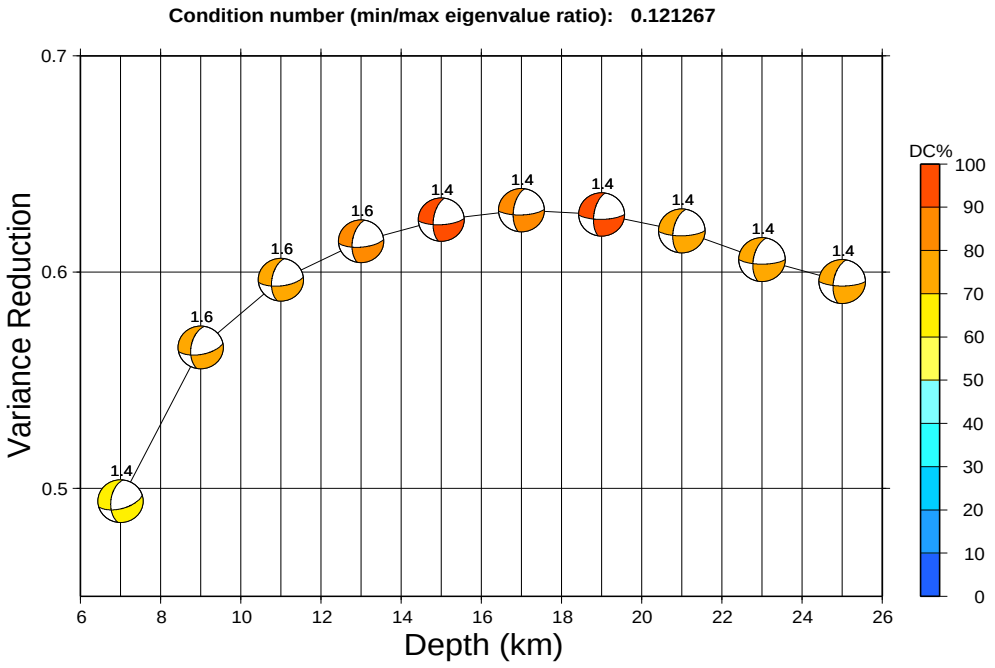

Figure 4.2: Variance reduction and focal mechanism as a function of depth. Beach balls are sized according to seismic moment. Colors represent the DC percentage. Numbers above beach balls express optimal time shifts.

from the inversion.

In step 3, working already without the NS component at KEK, we test trial subevent positions in a plane. We test both nodal planes of the optimum solution from step 2 because we do not know which of them is the fault plane.
Using empirical relations (Somerville et al., 1999) between the seismic moment and the area of the rupture (A) and the (total) area of asperities A_a we obtain A = 10 km^2 and A_a = 2.2 km^2; for details see Chapter 2.3. Study of such relatively small asperities would require fine sampling of the fault plane and relatively high frequency. Instead, we concentrate on a simpler task, to understand whether this earthquake actually follows the empirical relation between moment and A, or not, i.e., whether the main source contributions are concentrated in the area of the order of 10 km^2.

Consequently, the 25 trial source positions have the spacing DS = DD = 3 km, and the studied frequency range is 0.02-0.04-0.30-0.32 Hz. (Additional tests with a finer grid with DS = DD = 1 km, not presented here, provided the same results.)

For reasons of testing some criteria we compute both free- and fixed-mechanism inversion. In fixed-mechanism inversion we fixed the strike-dip-rake combination to the values 77, 72, -27 and seek only the position and time, for each subevent.

Formally, 5 subevents were retrieved, see Table 4.4 and Figure 4.5. Important positive feature of the solution is that the first (dominating) subevent went automatically in the position of the centroid point C, determined above, see Figure 4.6. This is an *a posteriori*

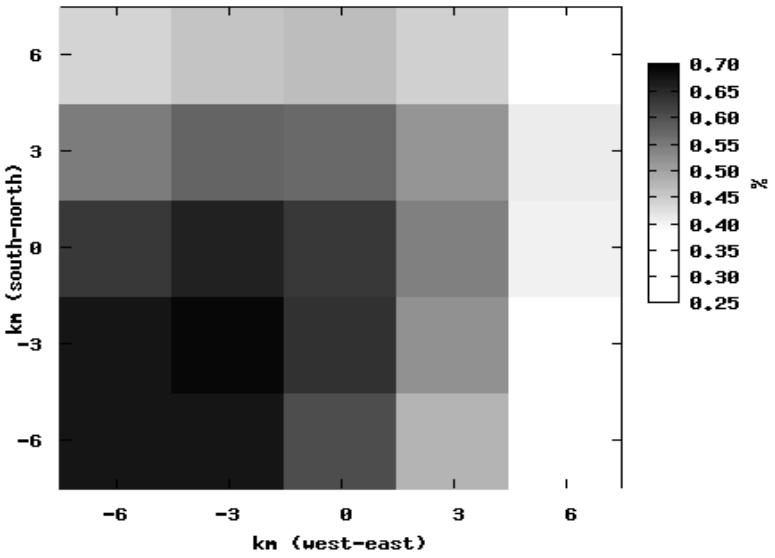

Figure 4.3: Amfilochia earthquake - horizontal plane in 17 km, maximum correlation for each position. Epicenter (SED) is in the center of the plane (position (0,0)), DX = DY = 3 km

verification of the depth and horizontal position of the centroid (retrieved independently in step 1 and 2, respectively). Correlation diagram for subevent 1 as a 2D function of the trial source position and time for free (deviatoric) and fixed mechanism moment tensor inversion are in Figure 4.7.
Next four subevents (subevent 2 to 5) are situated as shown in Figure 4.8 and Table 4.8. The resulting subevents are different for both nodal planes, but there are common features. Most importantly, for both planes we got two largest subevents of moments (0.9 and 0.5 $.10^{16}$ Nm), and they have the same relative distance (3 km from each other).
Finally, the most difficult part of the study is to determine which of the subevents are physically justified and which are just a numerical artifact (noise). To solve the problem, three different criteria are tested.

- Criterion 1: size of scalar moment - Table 4.4 and Table 4.5
  Optimally, the solution shows a few prominent subevents while the others are smaller (and comparable with each other). Such a drop in moment is not very clear in the studied case, nevertheless, it suggests that only 2 or 3 subevents are important when using nodal plane I or II, respectively.

  Summary moment of subevents is also interesting. (Employing free-mechanism inversion, we cannot sum up scalar moments of subevents, but their moment tensors and evaluate the norm of the sum.) For nodal plane II second and third subevent have comparable scalar moment but for the second subevent summary seismic moment increases and for third subevent decreases, see Table 4.6.

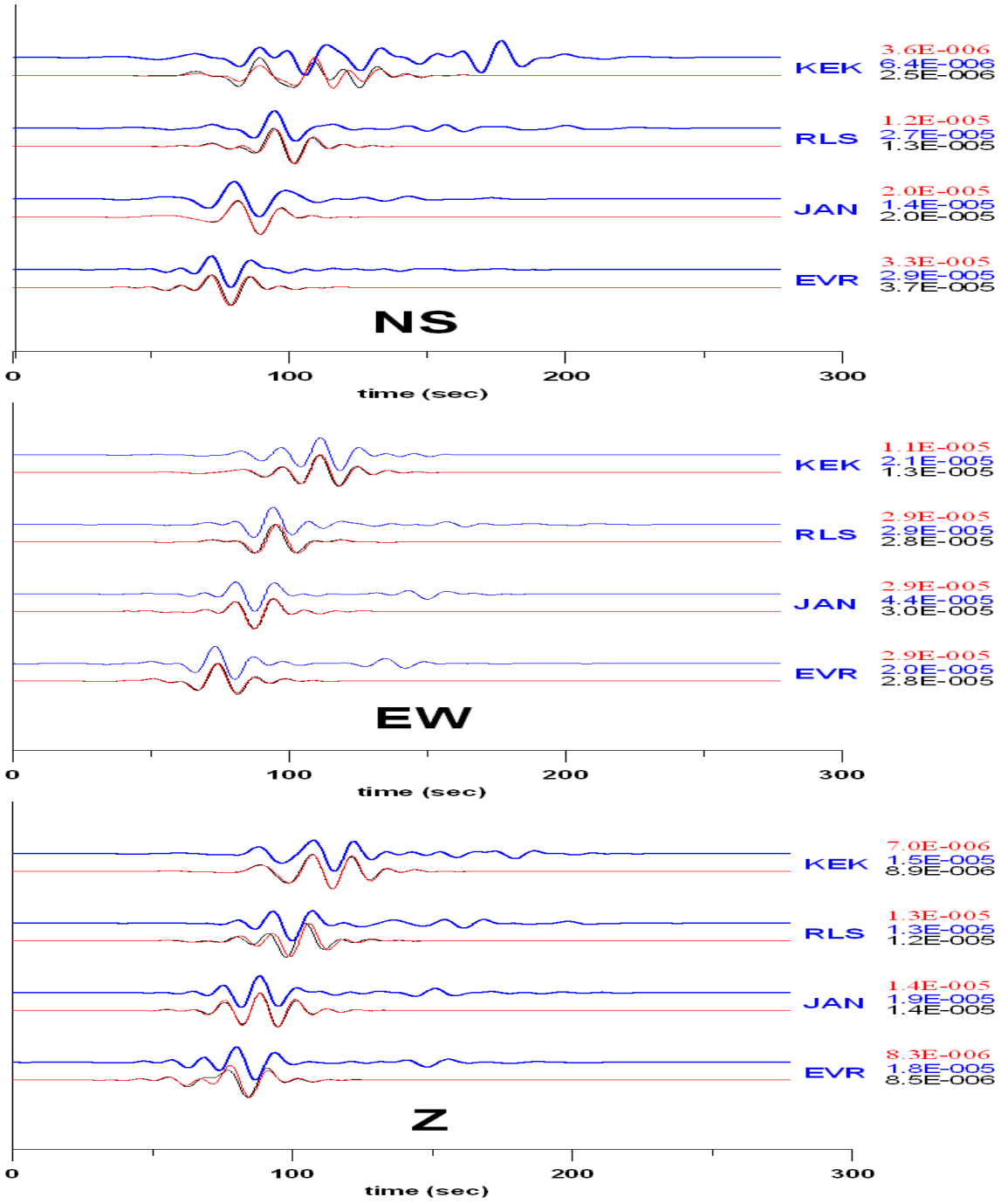

Figure 4.4: Amfilochia earthquake, point source waveform modeling, 0.04-0.08 Hz. Top (blue) - observed displacement, bottom - synthetic displacement for two solutions; for source position at hypocenter (black) or centroid (red). Numbers on the right-hand side are the peak values (in meters).

Seismograms include formal shift of 60 seconds

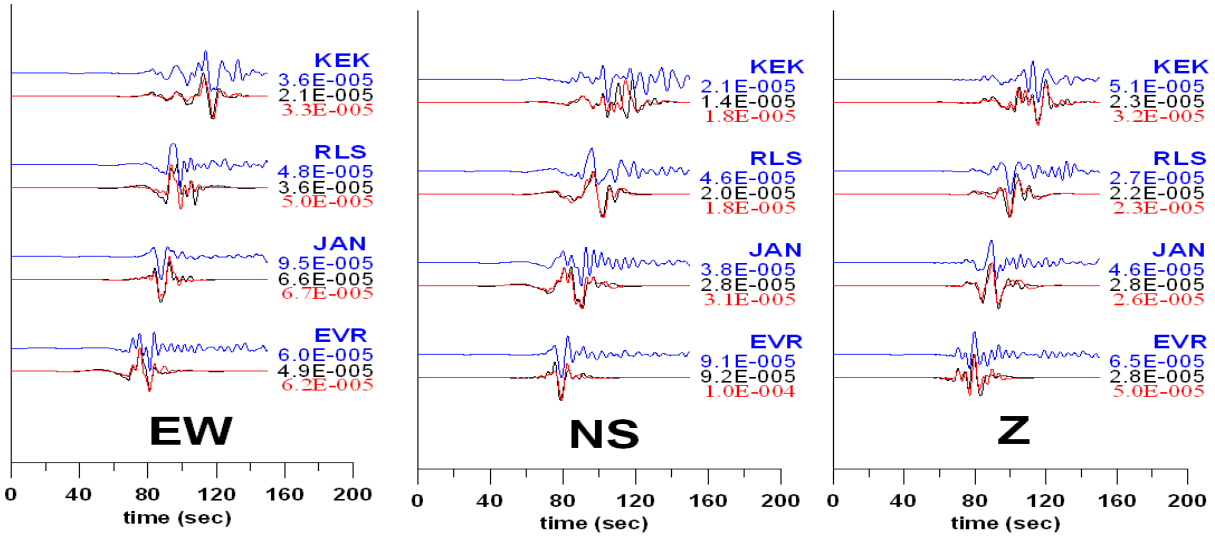

Figure 4.5: Amfilochia earthquake, multiple point solution, 0.04-0.3 Hz. Comparison between normalized data (top blue) and synthetics for 5 subevents (bottom black and red). The black curves are synthetics for nodal plane I (strike = 176), while the red curves are for nodal plane II (strike = 77).

Seismograms include formal shift of 60 seconds

- Criterion 2: consistency between fixed and free mechanism - Table 4.5
  - Stability of the solution is indicated if position and timing of subevents retrieved with free focal mechanism is similar to that retrieved with fixed mechanism.
  - Small variation in the mechanism from one subevent to the other is quite rare if the free-mechanism subevents are searched.

  Therefore, getting such a similarity and small variance in mechanism is a strong stability indicator. Such a test, made for nodal plane I (strike = 176), shows that mechanisms of the first and second subevents are indeed similar to the single source mechanism (from step 1 and 2, i.e. 77, 72, -27), thus indicating relevance of sub 1 and 2; see Table 4.5. For nodal plane II consistency is a bit lower. Mechanisms of first and second subevent is similar for free- and fixed-mechanism inversion. But position and scalar seismic moment for subevent 2 is different.

- Criterion 3: increase of variance reduction - Table 4.4
  Increase of the variance reduction from the first to the second subevent was relatively large, 7 to 8%, depending on the plane used. On the contrary, after the third subevent the variance reduction increased by 3% or less. Although we have no objective criterion how to stop the 'iteration process', this result indicates that the only relevant subsources are the first three.

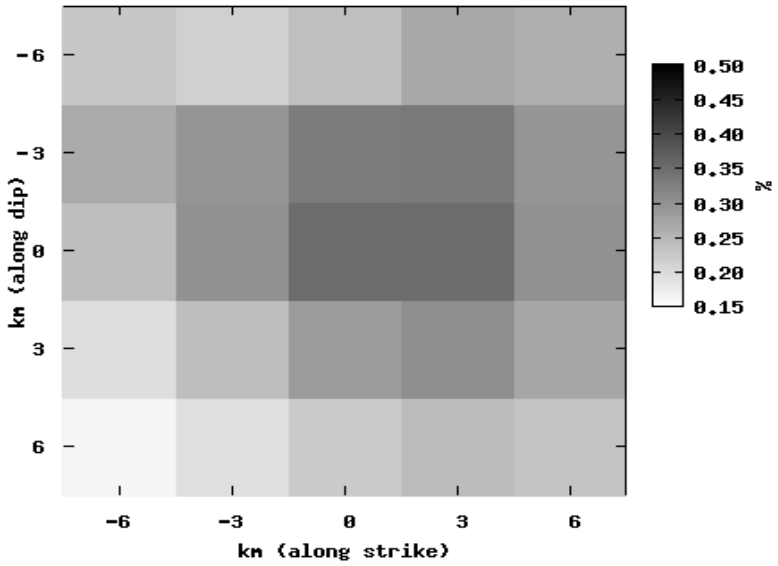

Figure 4.6: Amfilochia earthquake. Correlation diagram for nodal plane I (strike = 176). Maximum correlation for each position, in the center of plane is centroid position from step 2.

Nodal plane I (strike=176)

subevent	source position	time (sec)	moment (10^{15} Nm)	summary moment (10^{15} Nm)	variance reduction
1	I-13	0.8	8.68	8.68	0.36
2	I-18	3.0	5.25	13.93	0.44
3	I-8	8.4	2.04	15.97	0.47
4	I-1	1.8	1.61	17.58	0.50
5	I-10	11.4	1.57	19.15	0.51

Nodal plane II (strike=77)

subevent	source position	time (sec)	moment (10^{15} Nm)	summary moment (10^{15} Nm)	variance reduction
1	II-13	0.8	8.64	8.64	0.37
2	II-18	3.2	5.17	13.81	0.44
3	II-25	9.6	4.07	17.88	0.50
4	II-2	0.2	1.23	19.11	0.53
5	II-4	3.0	1.00	20.11	0.53

Table 4.4: Multiple point solution - 5 subevents from Figure 4.8. Note that only trial position no. 13 is common for both plane, e.g. position 18 for nodal plane I and II is different position. These source positions are shown in Figure 4.23.

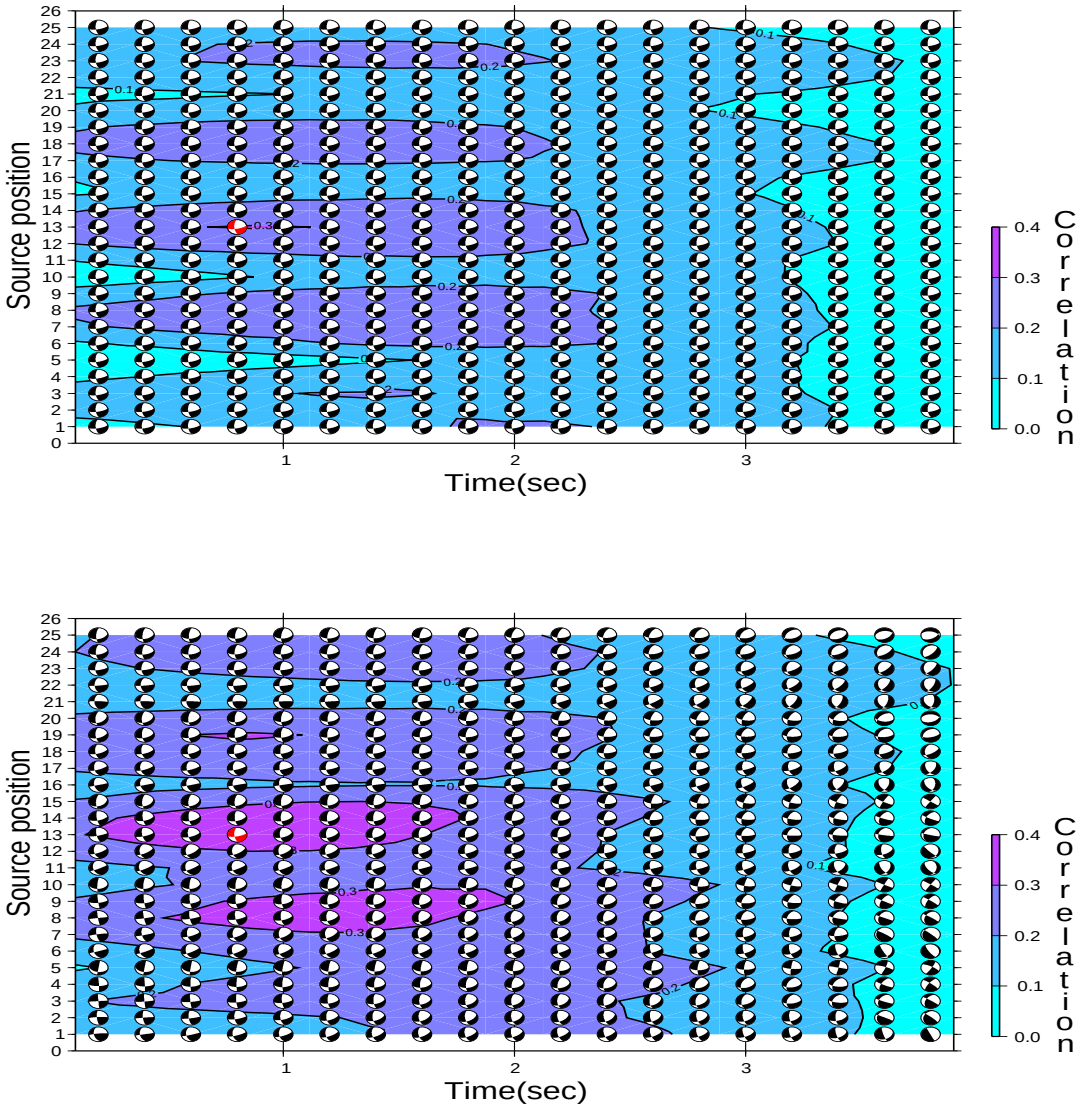

Figure 4.7: Amfilochia earthquake, correlation diagram for the first subevent 1 and nodal plane I (strike = 176). Top panel - fixed-mechanism inversion (deviatoric moment tensor); bottom panel - free-mechanism inversion.

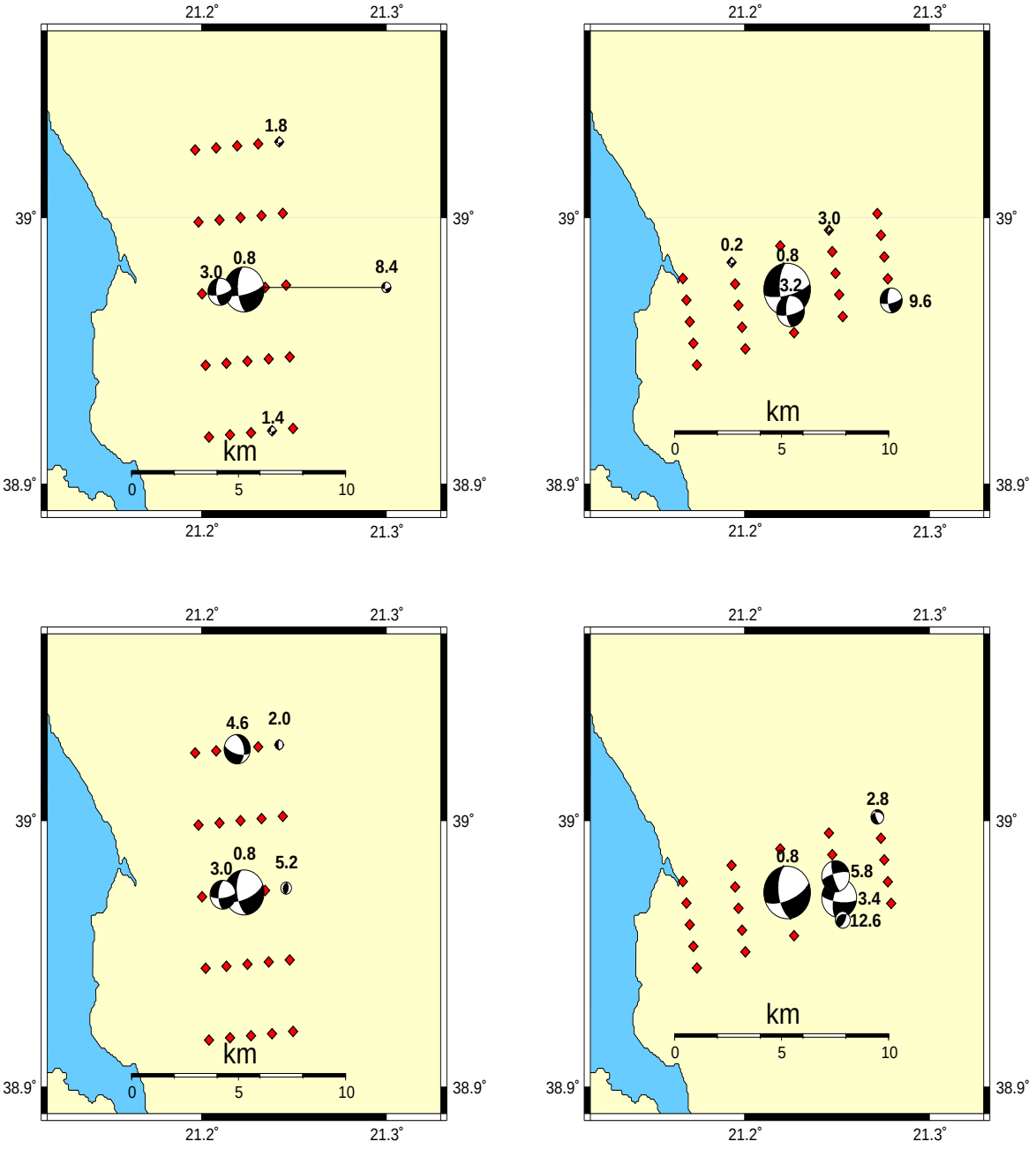

Figure 4.8: Amfilochia earthquake. Left top panel - multiple point solution for nodal plane I (strike= 176). Right top panel - for nodal plane II (strike= 77). Bottom panels - same as top panels, only with free-mechanism inversion. Red points are surface projections of the trial source positions (DS = DD = 3 km).

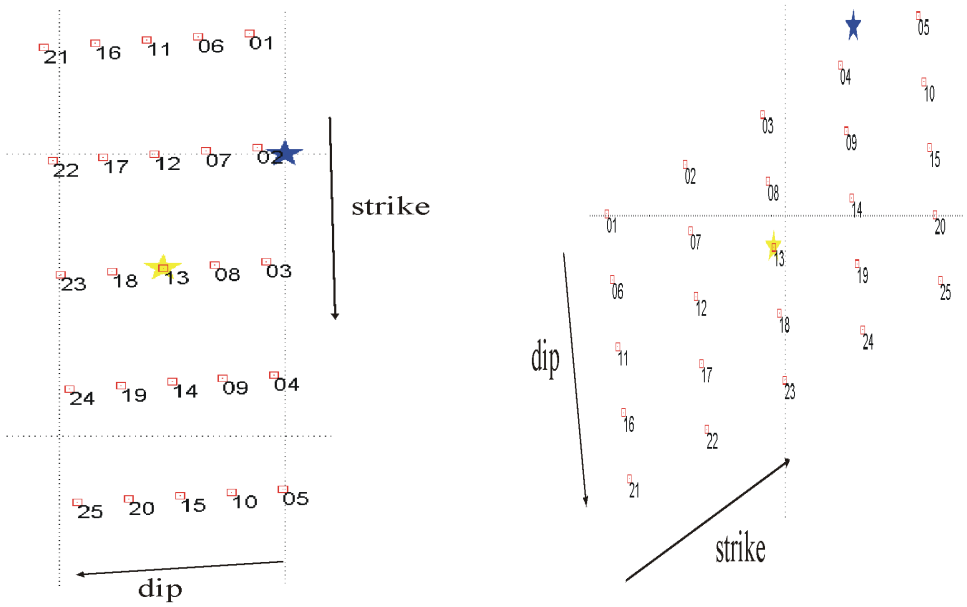

Figure 4.9: Amfilochia earthquake, surface projection of the trial source positions, blue star - centroid position from SED, yellow star - centroid position from step 2; blue star can be on the boundary of the grid (or outside this grid) because it was determine in different crustal model.

sub-event	source position	time (sec)	moment (10^{15}Nm)	summary moment (10^{15}Nm)	strike (deg)	dip (deg)	rake (deg)	strike (deg)	dip (deg)	rake (deg)	var. red. *)
1	I-13	0.8	8.65	8.65	68	66	-33	173	61	-152	0.38
2	I-18	3.0	5.50	13.37	83	72	-31	183	61	-159	0.47
3	I-11	4.6	5.67	12.25	106	63	-131	349	48	-37	0.54
4	I-3	5.2	2.28	10.79	8	53	89	190	37	92	0.56
5	I-1	2.0	1.8	11.94	19	13	-71	179	78	-94	0.59

Table 4.5: Amfilochia earthquake, free mechanism subevents for nodal plane I (strike = 176).

*) var. red. means variance reduction

sub-event	source position	time (sec)	moment (10^{15}Nm)	summary moment (10^{15}Nm)	strike (deg)	dip (deg)	rake (deg)	strike (deg)	dip (deg)	rake (deg)	var. red. *)
1	II-13	0.8	8.65	8.65	68	66	-33	173	60	-152	0.38
2	II-19	3.4	6.51	13.42	96	73	-27	194	65	-161	0.48
3	II-14	5.8	5.12	10.66	256	75	-166	163	77	-16	0.55
4	II-5	2.8	2.36	10.94	274	36	-151	160	73	-57	0.58
5	II-24	12.6	2.74	10.29	27	63	68	248	34	126	0.60

Table 4.6: Amfilochia earthquake, free mechanism subevents for nodal plane II (strike = 77).

*) var. red. means variance reduction

Relevance of the subevents was further tested by jackknifing. We repeatedly removed one from the four available stations, and recalculated the inversion. Fixed mechanism was used because the number of stations is low. As shown in Table 4.7, most robust subevents are 1 and 2.

sub-event	source position	time (sec)	moment (10^{15}Nm)	summary moment (10^{15}Nm)	reduction variation	omitted station
1	I-13	0.8	8.68	8.68	0.37	none
	I-13	1.0	9.77	9.77	0.38	EVR
	I-13	1.0	8.35	8.35	0.34	JAN
	I-13	0.6	8.06	8.06	0.37	RLS
	I-13	1.0	9.77	9.77	0.41	KEK
2	I-18	3.0	5.24	13.92	0.44	none
	I-18	3.2	6.88	16.65	0.48	EVR
	I-18	3.4	6.78	15.13	0.49	JAN
	I-18	3.0	5.17	14.94	0.45	KEK
	I-19	2.8	3.96	12.02	0.46	RLS
3	I-8	8.4	2.04	15.96	0.47	none
	I-8	8.4	2.14	18.79	0.49	EVR
	I-22	2.4	2.74	17.87	0.54	JAN
	I-13	8.4	2.75	14.77	0.48	RLS
	I-1	1.4	2.01	16.95	0.47	KEK
4	I-1	1.8	1.68	17.64	0.50	none
	I-6	13.8	1.87	20.66	0.50	EVR
	I-3	11.2	2.71	20.58	0.56	JAN
	I-6	1.4	2.27	17.04	0.54	RLS
	I-13	8.4	2.36	19.31	0.51	KEK
5	I-10	11.4	1.57	19.21	0.51	none
	I-21	1.6	2.29	22.95	0.52	EVR
	I-5	1.6	2.01	22.59	0.58	JAN
	I-15	11.2	1.48	18.52	0.55	RLS
	I-3	12.0	1.46	20.77	0.52	KEK

Table 4.7: Amfilochia earthquake - jackknifing for 5 subevents. For each subevent, the first row gives the inversion from 4 stations and the other rows represent the solution from three stations. Time of subevent is relative with respect to hypocentral time.

Summarizing all the tests, we conclude that the earthquake was composed from 2 subevents. Therefore, it is more likely that fault plane was nodal plane I. Seismograms for 2 subevents in nodal plane I are shown in Figure 4.10.

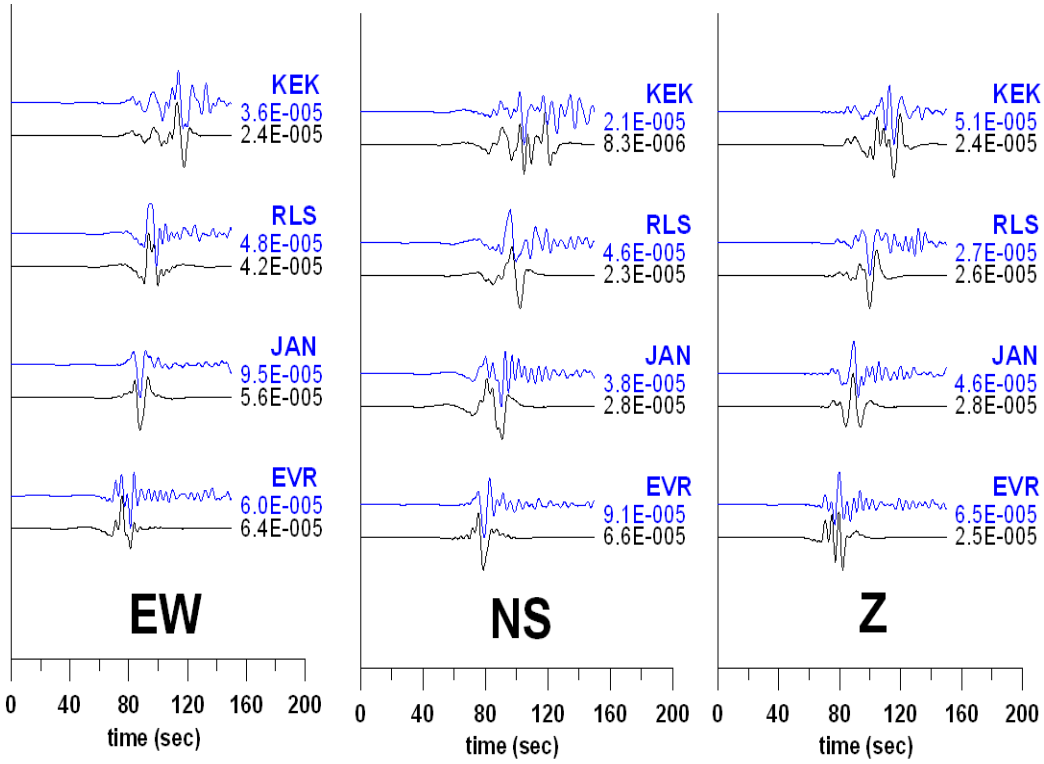

Figure 4.10: Amfilochia earthquake, two subevents for nodal plane I (strike = 176), source parameters are in Table 4.8, f = 0.04-0.3 Hz.

Seismograms include formal shift of 60 seconds

Polarity

Finally, we compare the focal mechanism obtained above from the waveforms with the observed first-motion polarities. Recall that the waveform inversion did not indicate any significant subevent preceding the major rupture (subevent 1). If, moreover, rupture is not much heterogeneous within subevent 1, we can expect agreement between the waveform-constrained mechanism of subevent 1 and the polarities. Indeed, such an agreement is documented by Figure 4.11.

As a result we got two subevents at nodal plane I situated 3 km and 2.2 sec from each other. For details see Table 4.8.

At the first glance our solution and solution from SED (or MEDNET) is different. We tested it with forward modeling of SED solution. Our solution was found at time around 1 second, we shifted our seismograms to the time t=0 sec because we want to see difference in mechanism. At most stations and components shape of synthetic seismograms are very similar. Main difference we see at KEK-NS but this component we reject by weights, that is why we can say nothing about this difference. Some small difference in shape of seismograms are at Z component, mainly at stations RLS and JAN. The changes in seismograms are very small, we cannot decide which solution is better, see Figure 4.12.

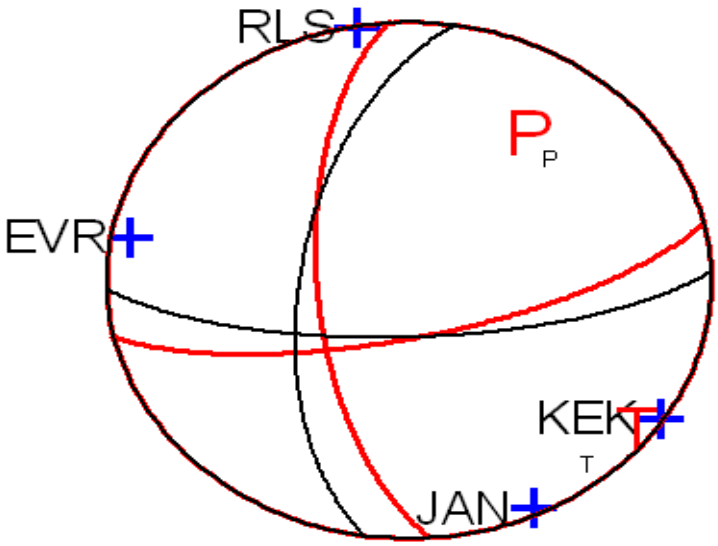

Figure 4.11: Amfilochia earthquake, black curve - mechanism from step 1, red curve - mechanism from step 2 (corresponding to centroid), blue signs - first-motion polarities.

sub-event	source position	time sec	x,N>0 km	y,E>0 km	z km	strike (deg)	dip (deg)	rake (deg)	moment (10^{15}Nm)	DC%
1	I-13	0.8	-3	-3	17	173	61	-152	8.65	19.1
2	I-18	3.0	-3.088	-4.265	19.719	183	61	-159	5.50	64.5

Table 4.8: Amfilochia earthquake, two subevents for nodal plane I, x,y,z are cartesian coordinates for each subevent. Position x=0 and y=0 is SED centroid position.

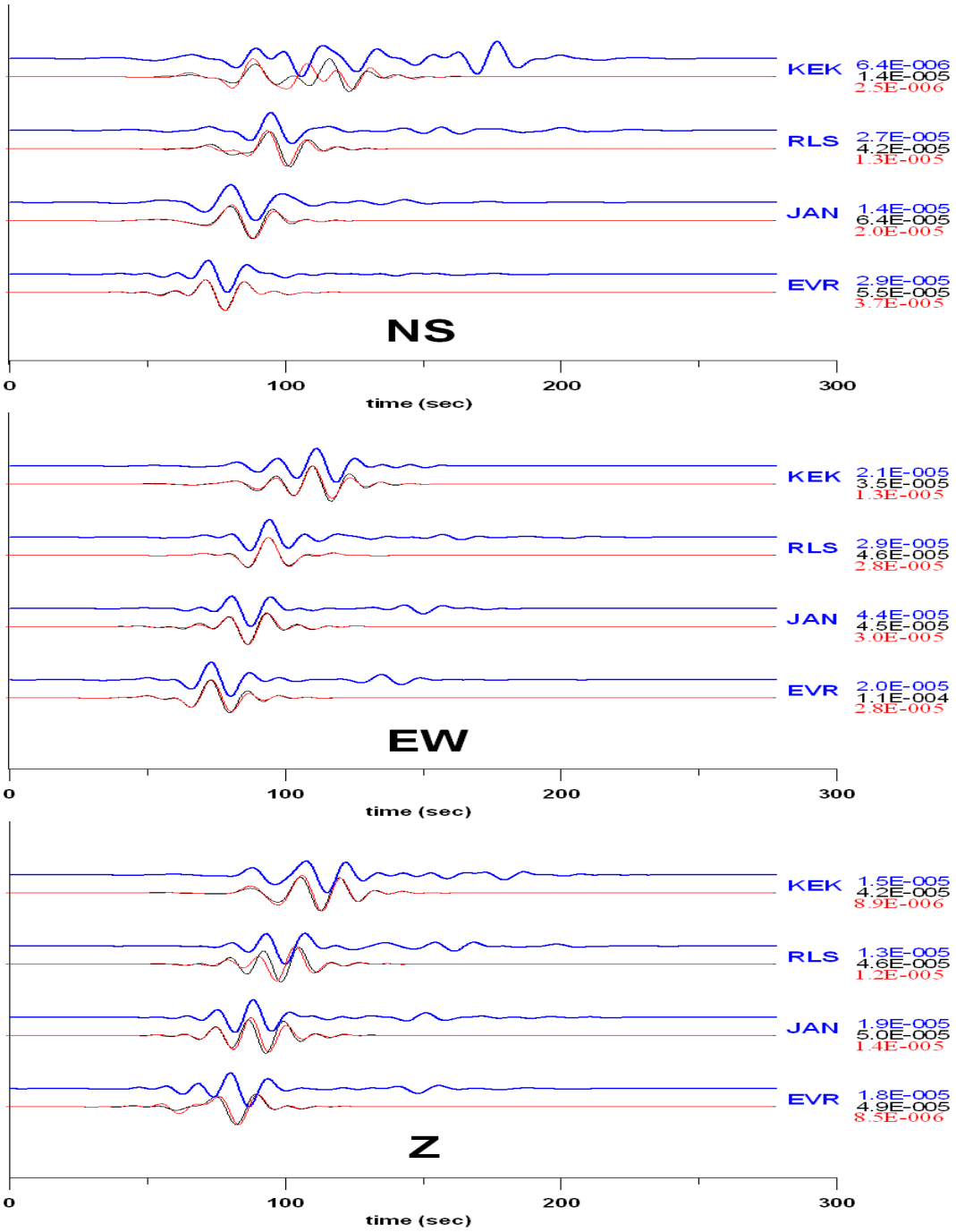

Figure 4.12: Amfilochia earthquake, Top (blue) - observed displacement, bottom - synthetic displacement for point solution from agency SED (black) and centroid solution (that from step 2) shifted to time t=0. sec (time that we found in point solution was t=1.4 sec)

4.2 Vartholomio earthquake

A moderate size earthquake $M_w \sim 5.5$ occurred near the town of Vartholomio, Western Greece, on December 2, 2002. Source parameters determined by five agencies are in Table 4.9.

agency	origin time (UTC)	lat.N (deg)	lon.E (deg)	depth (km)	M_0 (10^{17}Nm)	mag *)
SED +)	4:58:55	37.747	21.087	27	4.55	5.74
MEDNET +)	4:58:52.9	37.65	21.24	24	2.9	5.6
HARVARD +)	4:59:1.4	37.70	21.42	15	3.42	5.6
USGS-PDE	4:58:55.19	37.747	21.087	4	1.8	5.5
NOA	4:58:56.4	37.80	21.15	17		5.3

agency	strike (deg)	dip (deg)	rake (deg)	strike (deg)	dip (deg)	rake (deg)	DC%
SED	303	78	-14	36	77	-167	55
MEDNET	302	85	-10	33	81	-175	44
HARVARD	294	73	-36	36	56	-160	59
USGS-PDE	145	82	75	28	17	152	81

Table 4.9: Vartholomio earthquake, basic information from five major agencies.

*) Except NOA, 'mag' means the moment magnitude M_w. For NOA it means the local magnitude

+) origin time, latitude and longitude are for centroid

For this study we use six nearest broadband stations, see Figure 4.13. Five of them belong to the NOA network (RLS, VLS, ITM, EVR and KEK), and one station (SER) is jointly operated by the Charles University Prague and the University of Patras. Epicentral distance ranges from 40 to 250 km, see Table 4.10. Signal-to-noise ratio is good in frequencies as low as 0.04 Hz. The studied frequency band is 0.02-0.04-0.08-0.11 Hz for the single point solution, and 0.02-0.04-0.3-0.32 Hz for the multiple point solution. The Z component of the stations VLS, ITM and KEK is very noisy, and that is why we remove these three Z components by down-weighting in the point solution. For multiple point solution at higher frequencies we remove only Z component at station KEK.

At some stations and components, a long-period disturbance was found, that of the 'mouse-1' type (see Chapter 3). It was RLS-EW and RLS-NS (already detected in Zahradník and Sokos, 2004), ITM-EW, SER-EW and SER-NS. Correction (removal) of most of them was performed using method described in Chapter 3. Observed data for station RLS before and after removing 'mouse-1' type is shown in Figure 4.14. The only exception was the case of SER-NS, where the 'mouse' was not large, just comparable to the signal, thus hardly removable. That is why we reject that component by down-weighting, too. The RLS station is just the station from which we removed the large 'mouse' effect. We have some doubts about the quality of the mouse removal (see Figure 4.14), therefore we compute all

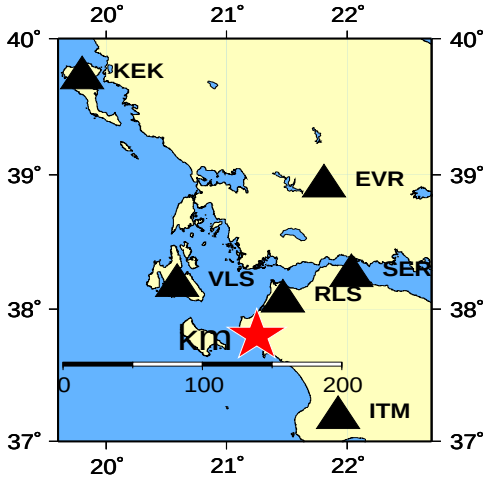

Figure 4.13: Vartholomio earthquake - red star: location from NOA, black triangles: stations used.

inversions with and without horizontal components of the station RLS.

station	distance (km)	azimuth (deg)
RLS	39.9	44.1
VLS	64.4	310.4
SER	92.2	57.1
ITM	97.2	134.9
EVR	137.7	24.5
KEK	242.7	331.5

Table 4.10: Stations used for the Vartholomio earthquake.

Single point solution

For waveform modeling, the crustal model of Haslinger et al. (1999) was used. We started from a single point solution (step 1 from Chapter 2.3), seeking it under the NOA epicenter between the depth of 5 and 50 km, with spacing DZ = 5 km. Then we continued with a finer spacing DZ = 2 km from 11 to 29 km. From this step we got the formal centroid depth of 17 km, but the resolution is low; see Figure 4.15.

In step 2 we fixed the depth of 17 km and used a 5 x 5 grid stencil of the trial positions in the horizontal plane; first with DX = DY = 5 km, and then refined to DX = DY = 3 km. Thus we got the centroid shift of 3 km to the east and 3 km to the north, see Figure 4.16. Improvement in the correlation between synthetics and data is 12% (from 52 to 64%). The main difference is on the Z component at the stations VLS and ITM. The focal mechanism

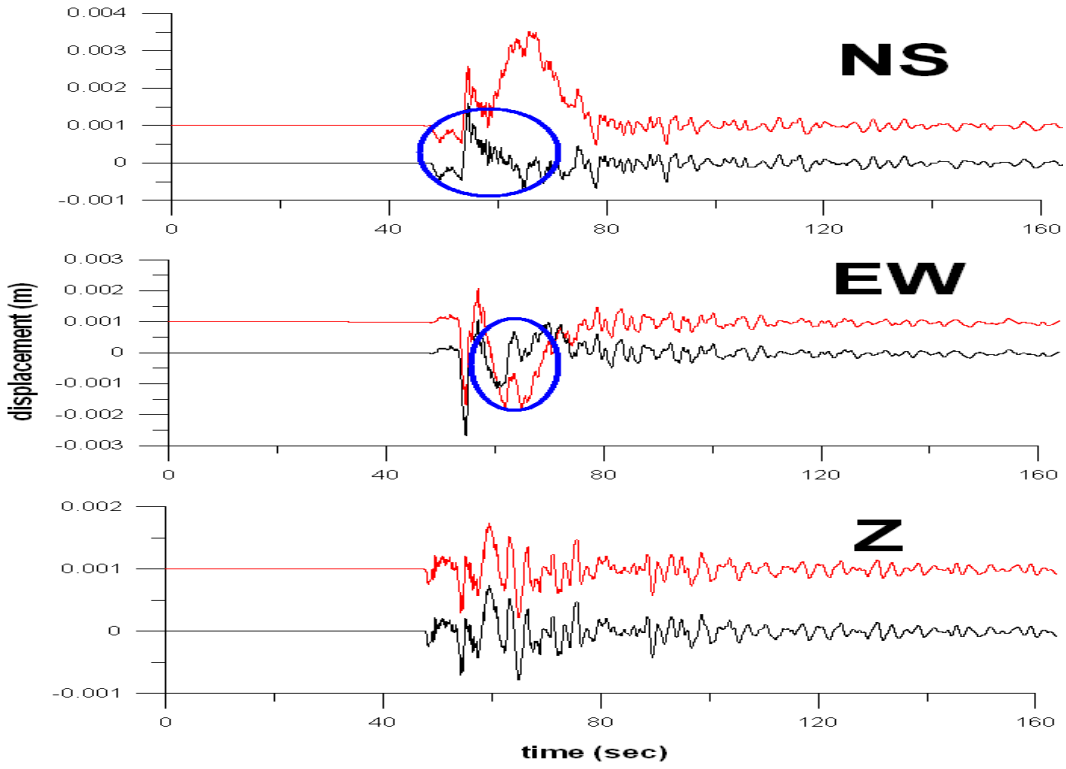

Figure 4.14: Vartholomio earthquake, black curves - non-filtered displacement after removing 'mouse-1 type' at NS and EW component (on figure is about one half of record in inversion). Red curves - non-filtered displacement before removing 'mouse-1 type', blue ovals - false pulses.

has changed: from 311, 87, 13 (220, 77, 177) in step 1, to 314, 65, 13 (219, 78, 154) in step 2.

Recalling that the crustal model of Haslinger et al. (1999) was not derived particularly for the studied region, we should count with possible misfits due to improperly modeled crustal propagation. Indeed, Figure 4.17 shows that at most stations and components the data and synthetics agree in their shape and show only apparent temporal shifts. Therefore, before going into a more detailed source analysis in the following steps, we should solve this problem. One possibility would be to derive a better crustal model for this area. This is left for future work. Another approach, applied here, is to formally shift the data to better align with the synthetics. Shifts are different for different stations and components, ranged from 1 to 5 seconds to the right or to the left.

Then we recompute step 1 and 2 and ask how large is the difference. The result is that with the shifts we get the same centroid position as that without the shifts. The correlation is very similar to that without shifts (62%). The focal mechanism has changed from 314, 65, 13 (219, 78, 154) without shifts to 312, 69, 13 (217, 78, 159) with the shifts in step 2. Scalar seismic moment is $M_0 = 1.48.10^{17}$ Nm without shifts of data and $M_0 = 1.55.10^{17}$ Nm with shifts. Stability like that is understood as encouragement to perform the following, more detailed, analysis with the formal shifts. If we have good low-frequency signal (up to 0.08 Hz) we can use the same shifts at higher frequencies. In

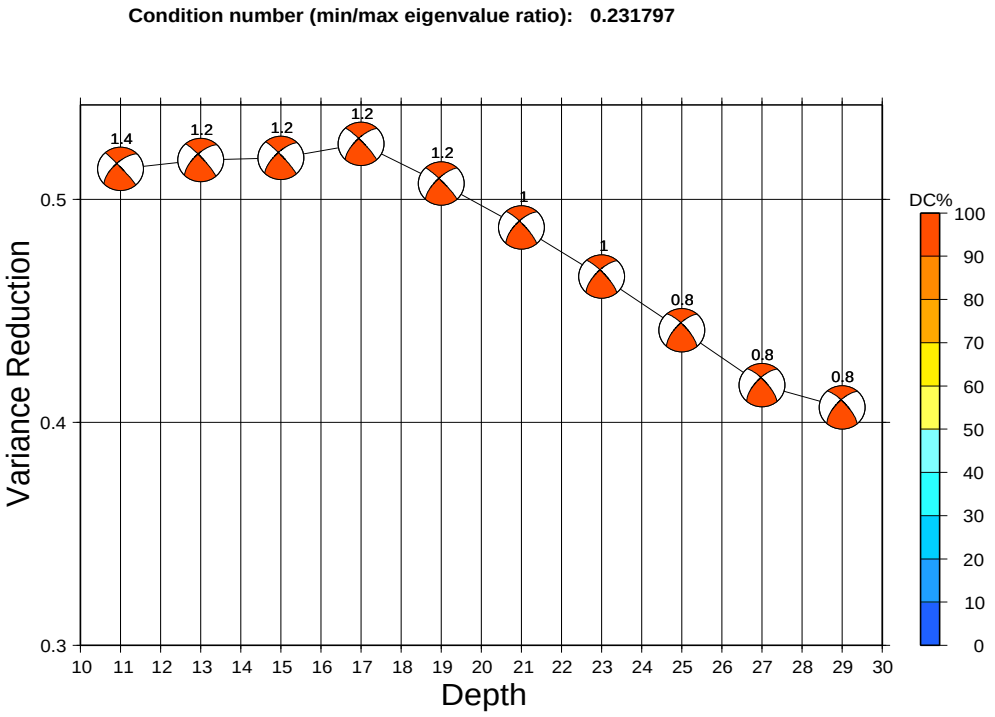

Figure 4.15: Vartholomio earthquake, variance reduction and focal mechanism as a function of depth. Beach balls are sized according to seismic moment. Numbers above beach balls express optimal time shifts.

case that we have no low frequency signal, the data up to 0.08 Hz and up to 0.3 Hz are very different (e.g. on Z component at stations VLS, ITM and KEK; see Figure 4.18), hence the shifts cannot be used.

Independent justification for the shifts is that forward modeling in various crustal models produces time shifts of several order of magnitude; see Figure 4.19.

Multiple point solution

In step 3 (from Chapter 2.3) we continue with multiple point solution in the frequency range 0.02-0.04-0.3-0.32 Hz. From empirical relations (see Chapter 2.3), and using M_0 (SED), we got rupture area $A = 61$ km^2, and the area covered by asperities $A_a = 13$ km^2. Using M_0 (USGS-PDE) we got $A = 35$ km^2 and $A_a = 7$ km^2. Therefore, with maximum frequency 0.32 Hz, the point source approximation for the asperities still holds. To find asperity(-ies), the spatial step of the order of $\sqrt{13} = 3.6$ km (or $\sqrt{7} = 2.6$ km) is adequate. We tested both nodal planes using 25 trial source positions, DS = DD = 3 km.

From the first calculation with both nodal planes we did not get the first subevent in the previously determined centroid position. Instead, the position of the formal maximum of the correlation was on the boundary of our tested grid stencil. This subevent had very similar mechanism to that in centroid position: 323, 72, 24 (225, 66, 160).

On the other hand, the preferred position on the boundary of the studied grid improves the correlation only by 2% compared to the former centroid position. To understand better

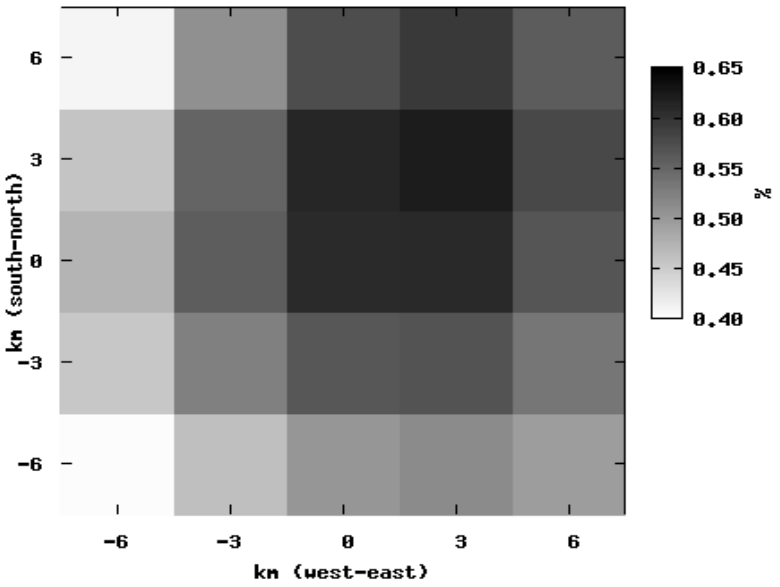

Figure 4.16: Vartholomio earthquake, correlation diagram for horizontal plane in the depth of 17 km, optimum correlation for each position. In the center of the plane is the centroid position from step 1. New centroid position from this step 2 is marked by the darkest grey (3 km to the east and 3 km to the north).

whether to use this new centroid position, or to keep the former one, we made forward modeling of the two cases and compared the results. The differences were very small at all stations and components. Shapes of synthetic seismograms are very similar, small changes are in amplitude. Generally amplitude for centroid position are smaller than observed while for "new position" larger.

Formally, we searched for 3 subevents. Subevents 1 and 2 have similar mechanism. For subevent 2 we got mechanism with rake turning round 180 degree. We manually change time of this subevent and then we got mechanism similar to subevent 1. For subevent 3 the second maximum with mechanism same as subevents 1 and 2 is very slight, therefore we cannot choose this maximum.

For the second and third subevent, variance reduction increases very slowly (up to 1%). Correspondingly, there is no "visible" difference between synthetic seismograms for one or three subevents. These three (formal) subevents are shown in Table 4.11. We also tried to test stability by removing some stations. We found out that these subevents are very unstable in mechanism, position and time. Therefore, we trust only the first subevent.

There are two possible interpretations of this result:
a) the earthquake had simple character, just one asperity, or,
b) it was more complex, but we are unable to detect the complexity by our simple approach.

To decide between these two, we analyze the agreement between observed and synthetic data in Figure 4.20 in more detail.

The variance reduction in Table 4.11, determined as a single number from all stations and all components is very low. On the other hand, if we recompute variance reduction for each station and component separately, for many components we find a good fit, see

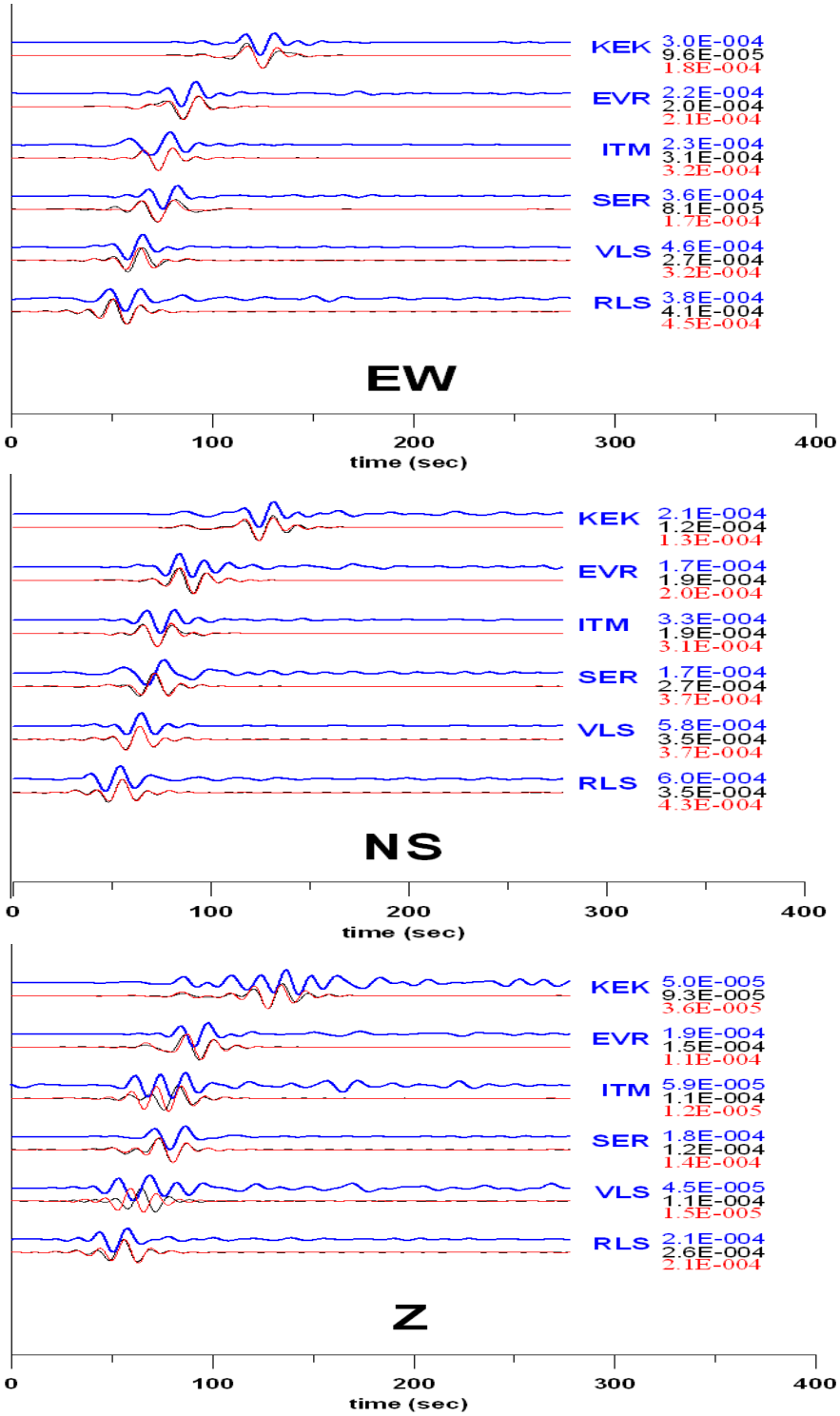

Figure 4.17: Vartholomio earthquake, the point source waveform modeling, 0.04-0.08 Hz. Top (blue) curves - observed displacement, bottom curves - synthetic displacement for two solutions; with (black) and without (red) the centroid shift. Numbers on the right-hand side are the peak values (in meters). Components SER-NS, VLS-Z, ITM-Z and KEK-Z were not used in inversion.

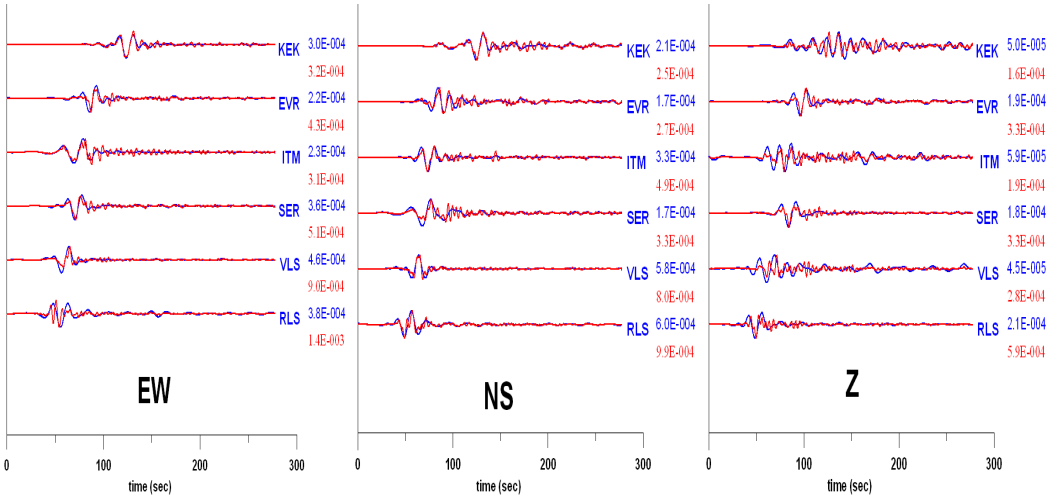

Figure 4.18: Vartholomio earthquake, observed data in two frequency ranges: 0.04-0.08 Hz (blue) and 0.04-0.3 Hz (red).

Table 4.12. The worst fit is for RLS, SER-NS, SER-Z, ITM-EW, KEK-Z. Horizontal components at station RLS and SER-NS we didn't use in inversion that is why variance reduction for them is very low. At ITM-EW we have disagreement in shape of seismogram, especially in width of synthetic seismogram. It can be caused by e.g. focal mechanism, crustal model, etc. At KEK-Z is very bad signal-to-noise ratio and at SER-Z is this ratio better than for KEK-Z but it is not optimal. Before this computation we thought that there is no problem with SER-Z. We analyze this record more detailed for frequency band 0.04-0.3 Hz and we found out that signal for this component is not as good as for the other stations and components. We can explain all 'bad' components that is why we expect very low variance reduction for these components. For next earthquake we should compute variance reduction for each component separately because it can detect some instrumental problem or problem with noise.

We cannot claim that earthquake consists of just 1 asperity. Rather it is more complex but we fail resolving the detailed source structure. Zahradník and Sokos (2004) found 3 nearby but enough delayed subevents. We didn't test exactly this configuration but in some testing we got similar difference in time.

sub-event	time (sec)	moment (10^{16}Nm)	summary moment (10^{16}Nm)	strike (deg)	dip (deg)	rake (deg)	strike (deg)	dip (deg)	rake (deg)	var. red. *)
1	2.4	10.5	10.5	308	89	7	218	83	179	0.27
2	-1.0	5.10	14.0	335	77	4	244	86	167	0.28
3	7.8	3.6	11.0	144	75	180	234	90	15	0.29

Table 4.11: Vartholomio earthquake, free mechanism subevents for nodal plane FII (strike = 217). Subevents are in different positions.

*) var. red. means the variance reduction

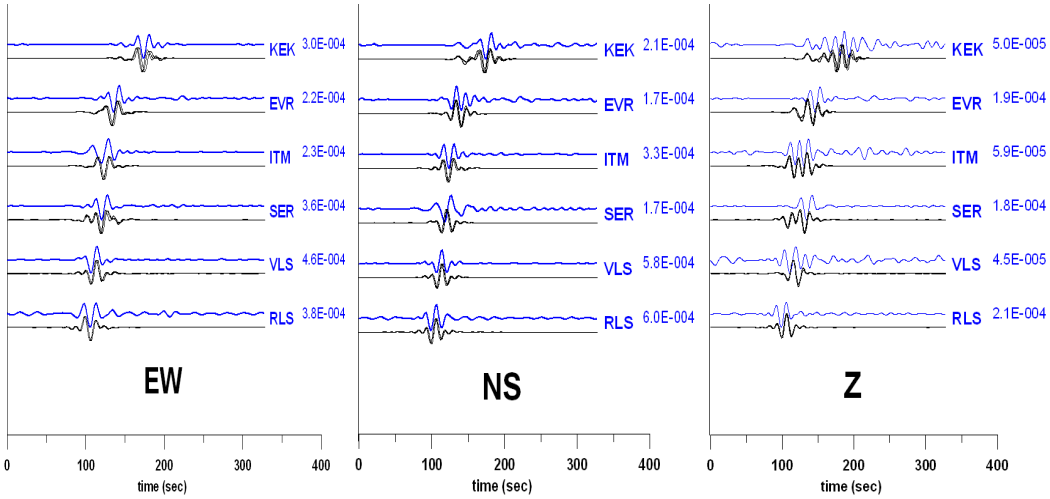

Figure 4.19: Vartholomio earthquake, top blue curves - observed displacement, bottom black curves - synthetic displacement for several crustal model in centroid position, f = 0.04-0.08 Hz.

station	NS (%)	EW (%)	Z (%)
RLS	x	16.17	2.99
VLS	52.97	42.04	40.58
SER	x	49.59	x
ITM	59.4	x	20.72
EVR	34.98	42.45	30.5
KEK	38.65	38.28	x

Table 4.12: Vartholomio earthquake, variance reduction for each station and component separately.

'x' means a very wrong fit, the variance reduction falls to negative values.

Comparison with centres

Our solution agrees with big centers in strike, dip and rake. In seismic moment, there are differences from $1.8.10^{17}$ Nm (USGS-PDE) to $4.55.10^{17}$ Nm (ETH). Our moment ($1.55.10^{17}$ Nm) is near to the solution from USGS-PDE, but that solution has mechanism different from all other agencies. We got approximately one half of mechanism reported by agencies. Roumelioti et al. (2004) obtained similar moment as us ($1.89.10^{17}$ Nm). This disagreement requires more detailed study, it is some general problem of this method.

Geometry hypocenter - centroid - nodal planes

We try to determine fault plane from geometry of hypocenter and centroid. We assume that these two points lie in the fault plane and it should be one of the nodal planes. We use hypocenter from NOA agency and centroid position from step 2. We work in several step in Cartesian coordinate system with origin in NOA epicenter (we can choose arbitrary origin). We make 3D plot of both nodal planes passing through centroid. From Figure 4.21 we see that only for nodal plane II hypocenter and centroid lie in one plane (i.e. in one

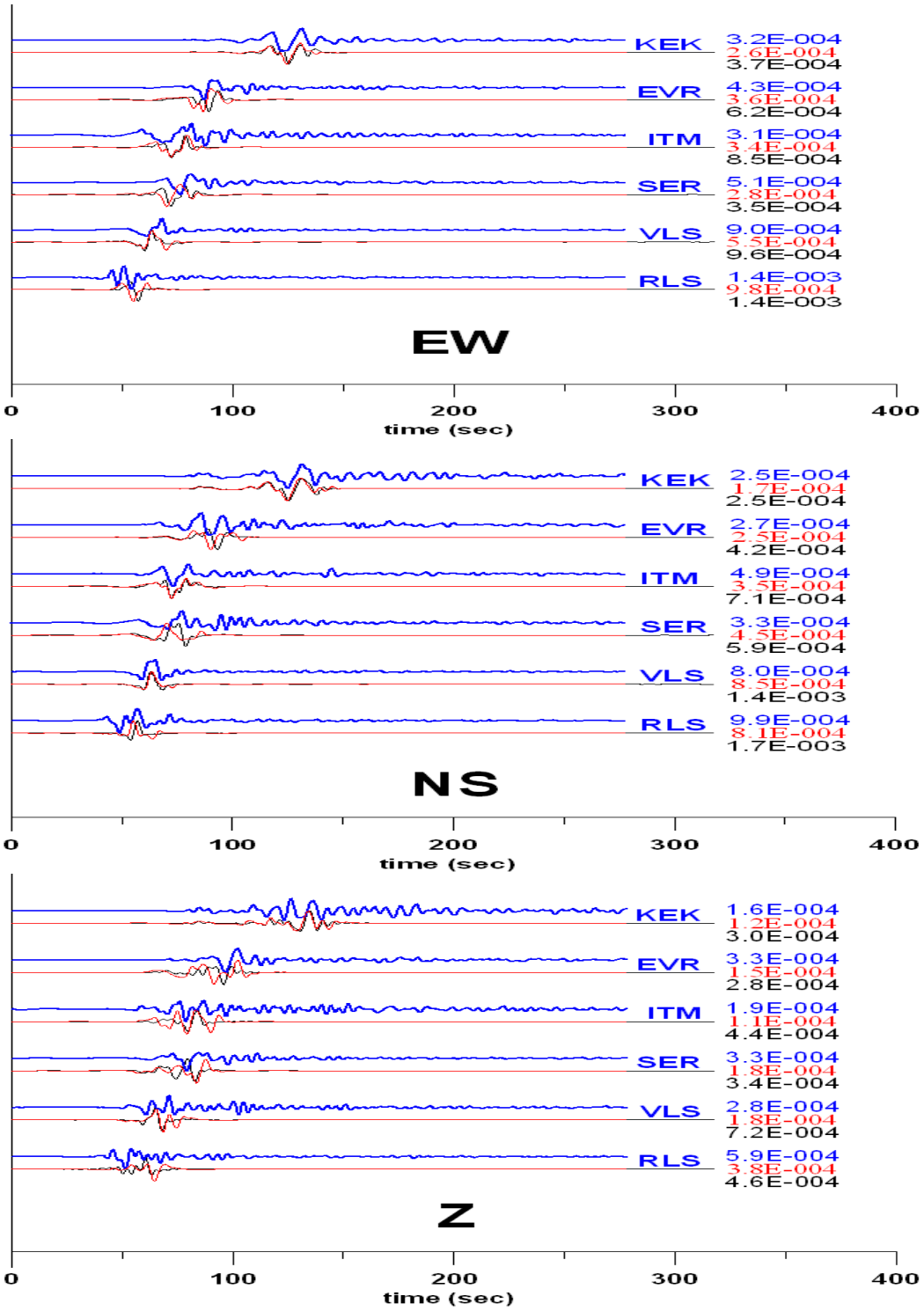

Figure 4.20: Vartholomio earthquake, top (blue) curves - observed filtered (0.04-0.3 Hz) displacement with shifts from single point solution, bottom curves - comparison between 3 subevents compute with ISOLA (red) and extended finite source (black).Components SER-NS and KEK-Z were not used in inversion.

from two nodal planes). Figure would require error bars in the hypocenter and centroid position, but we don't know them. Generally, the largest location error is in depth. The hypocenter depth of 17 km agrees with nodal plane II, while for nodal plane I we would need the depth around 5 km. We assume that error larger than 10 km is unlikely for this event. Therefore, we preliminary conclude that fault plane was nodal plane II. To further justify this interpretation, we have to make new relocation of the hypocenter in the same model as that used for the centroid location (Zahradník, personal comm.). This is left for future work. There was some aftershocks but verification by them is impossible at this moment because we didn't know locations of them.

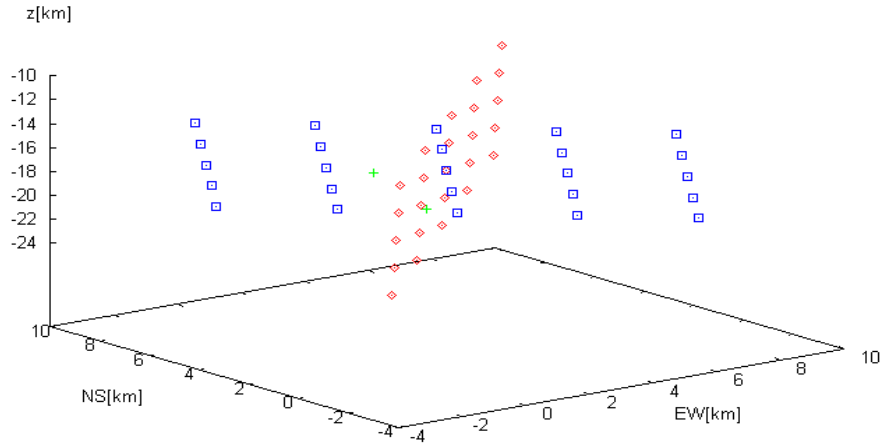

Figure 4.21: Vartholomio earthquake, geometry of nodal planes, blue points - nodal plane I, red point - nodal plane II, green points - old position on nodal plane II and new position on nodal plane I.

Extended source

For the largest frequency of 0.3 Hz, the wavelength is 9 km. This is comparable with size of the fault area (8 x 8 km). Therefore, we tried to model this earthquake also with the finite-extent source. We employed the centroid position from step 2 (3 km to the north and 3 km to the east from NOA epicenter) and nodal plane II with strike-dip-rake combination 217, 78, 159. Further we assume slip distributed in a circle centered in the centroid, radius = 2.5 km (from empirical relation). Hypocenter at depth 17 km, for detail geometry see Figure 4.22. First results for finite source are shown in Figure 4.20. Globally, this solution is not better than the previous point solution(-s). We must study the centroid-hypocenter geometry in more detail (relocate hypocenter in Haslinger et al. (1999) crustal model, compute centroid with small spatial step, recompute all in other crustal model, etc.). This is left for future study.

Because we are not satisfied neither with multiple point solution nor with extended source we try change centroid position and recompute multiple point solution for nodal plane I (strike = 312). After some testing in which profitted from a fortunate mistake

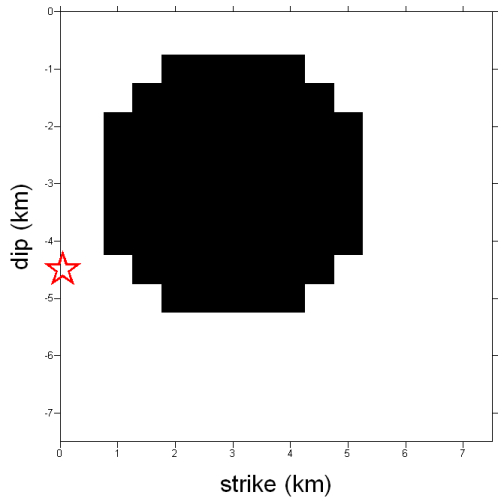

Figure 4.22: Vartholomio earthquake, red star - hypocenter, black circle - asperity with radius 2.5 km and with constant slip distribution $\Delta u = 0.45$ m.

we got better results in "new centroid position" with coordinates x(NS) = 3 km and y(EW) = -3 km, see Table 4.13 and Figures 4.24 and 4.25. In case without weights the main difference is at RLS-NS where we explain the first pulse with subevent no. 3 (we know this from forward modeling each subevent separately). Times of subevents with and without weights are different but in similar positions (except subevent 2 in case without weights, where the resolution in all directions was very low). Main difference is in the depth of subevents but resolution in depth is very low. First three subevents have very similar mechanism (in both cases with/without weights). Variance reduction increases for first three subevents (with weights) and for all 5 subevents (without weights). Therefore we trust first three subevents but it needs more detailed study (similar to that from previous section - jackknifing, test with free- and fixed-mechanism inversion, etc.; it is left for future study). Summary seismic moment of these three subevents $1.54.10^{17}$ Nm agrees with scalar seismic moment from point solution ($1.55.10^{17}$ Nm). Seismograms for five subevents with and without weights are shown in Figure 4.26, distribution of subevents for both case is in Figure 4.27.

From geometry "new centroid" x hypocenter we got fault plane as nodal plane I (strike = 314), for centroid from step 2 it was nodal plane II. Extended source for "new centroid position" is left for future study.

Polarity

We read first-motion polarity from all stations, see Figure 4.28 and compared with centroid solution. Station VLS is situated near one of the nodal plane. At Z component polarity is very bad discernible, but horizontal components help to determine first-motion polarity for this station. Then, with no doubt, we can say that at VLS station the polarity disagrees with the centroid solution.

This disagreement cannot be caused by difference between H (hypocenter) and C (centroid) position, or wrong hypocenter determination. (We tested depths from 5 to 30 km and in horizontal components up to 5km to each side.) On the other hand, small change

Without weights

sub-event	source position	time (sec)	moment (10^{16}Nm)	summary moment (10^{16}Nm)	strike (deg)	dip (deg)	rake (deg)	strike (deg)	dip (deg)	rake (deg)	var. red. *)
1	11	1.0	8.7	8.7	216	70	164	312	75	21	0.24
2	24	6.8	5.5	12.0	29	73	161	125	72	18	0.28
3	16	-3.8	5.2	15.4	10	85	-164	279	74	-5	0.32
4	12	3.0	3.3	18.2	214	87	-174	124	84	-3	0.36
5	23	15.4	4.6	21.6	130	60	-5	223	86	-150	0.39

With weights

sub-event	source position	time (sec)	moment (10^{16}Nm)	summary moment (10^{16}Nm)	strike (deg)	dip (deg)	rake (deg)	strike (deg)	dip (deg)	rake (deg)	var. red. *)
1	11	1.4	6.8	6.8	218	85	-179	128	89	-5	0.12
2	11	-1.2	4.8	12.0	231	70	160	328	71	21	0.21
3	12	4.0	4.6	15.4	231	73	176	322	86	17	0.29
4	14	11.2	3.7	15.7	270	67	-29	12	64	-154	0.28
5	6	7.2	2.7	13.5	147	85	-177	57	87	-5	0.27

Table 4.13: Vartholomio earthquake, free mechanism subevents for nodal plane I (strike = 314) in "new centroid position"; trial source positions are shown in Figure 4.23.

*) var. red. means the variance reduction

in mechanism around 5 degree in strike can explain the VLS disagreement (we know that 5 degree difference is easy to obtain, e.g. by a small change in weights). Another crustal model can also produce such small change.

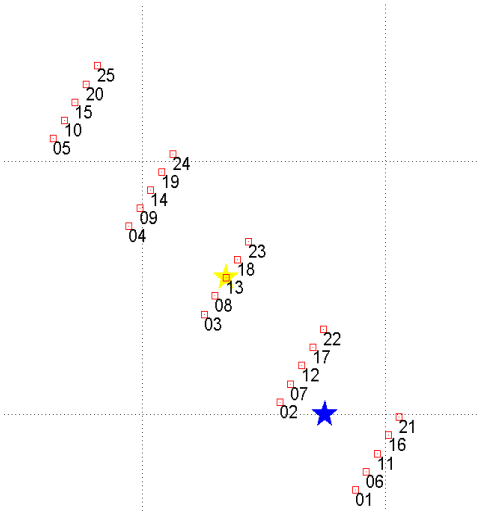

Figure 4.23: Vartholomio earthquake, trial source positions in nodal plane I, blue star: NOA hypocenter, yellow star: "new centroid position".

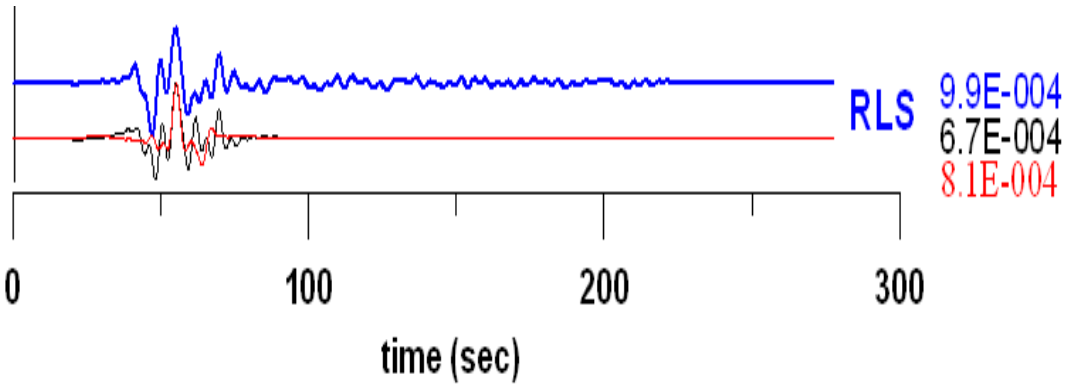

Figure 4.24: Vartholomio earthquake, station RLS, NS component. Blue curve - observed displacement, black curve - synthetic seismogram for 5 subevents in "new centroid position", red curve - synthetic seismogram for 3 subevents in old centroid position, f = 0.04-0.3 Hz. Components SER-NS and KEK-Z were not used in inversion.

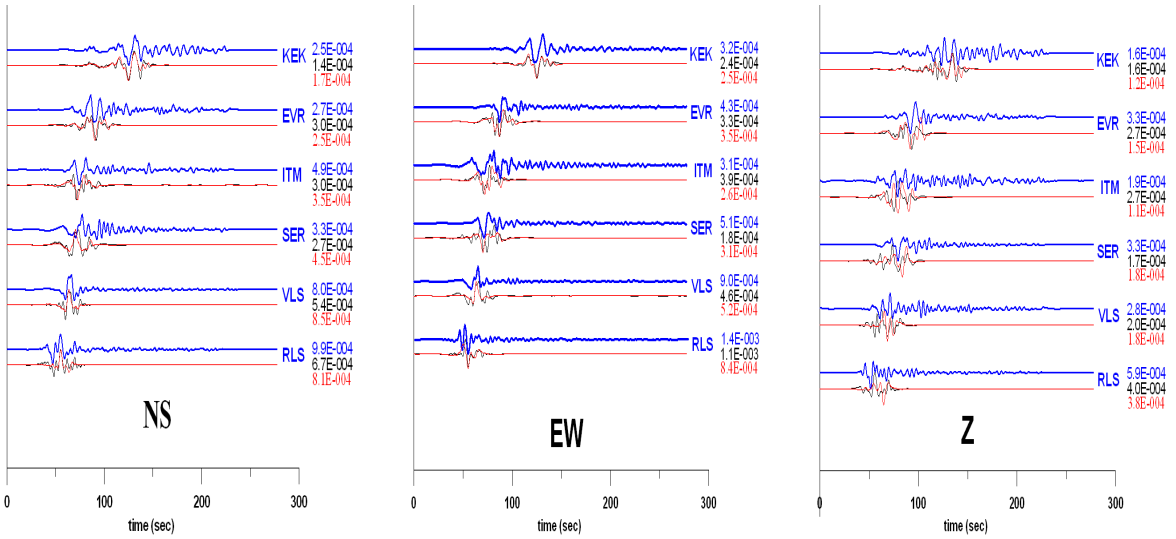

Figure 4.25: Vartholomio earthquake, the same as Figure 4.24, only for all stations and components, f = 0.04-0.3 Hz. Components SER-NS and KEK-Z were not used in inversion.

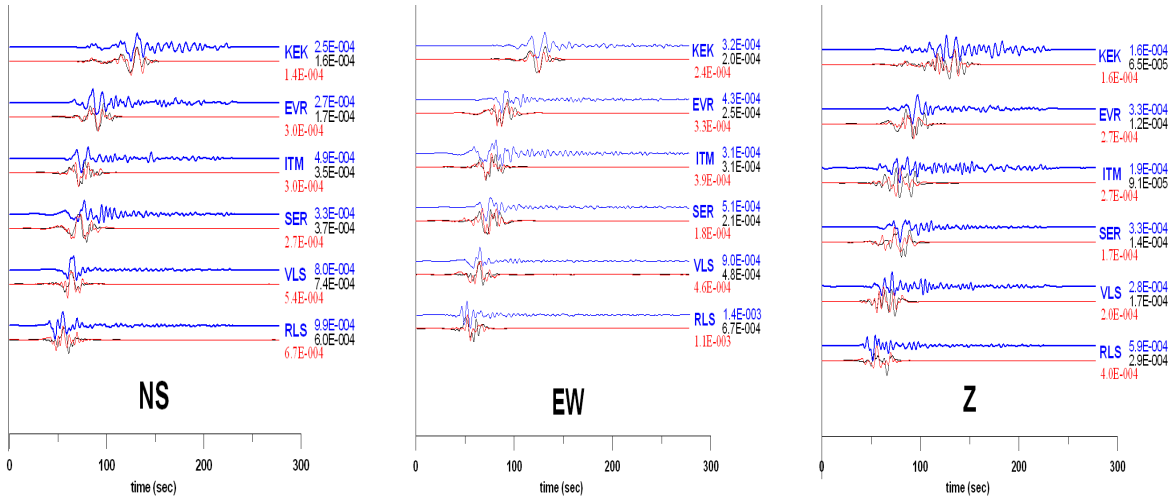

Figure 4.26: Vartholomio earthquake, Top (blue) curves - observed displacement, bottom curves - synthetic displacement for two solutions with 5 subevents; with (black) and without (red) weights in inversion. Numbers on the right-hand side are the peak values (in meters). Components SER-NS and KEK-Z were not used in inversion; f = 0.04-0.3 Hz.

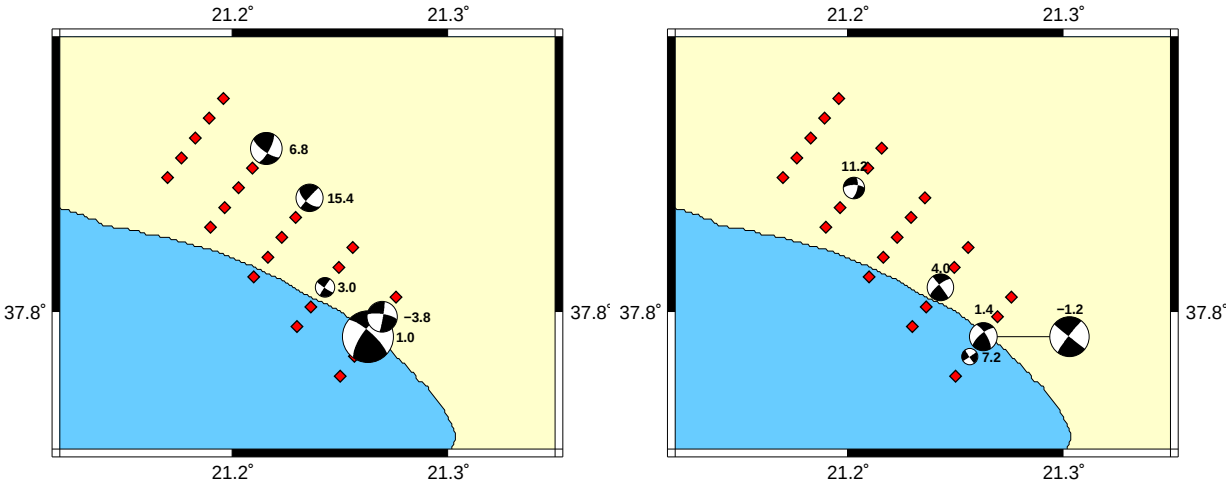

Figure 4.27: Vartholomio earthquake. Left panel: multiple point solution for nodal plane I (strike = 312) without weights. Right panel: same as left panel only with weights. Red points are surface projections of the trial source positions (DS = DD = 3 km).

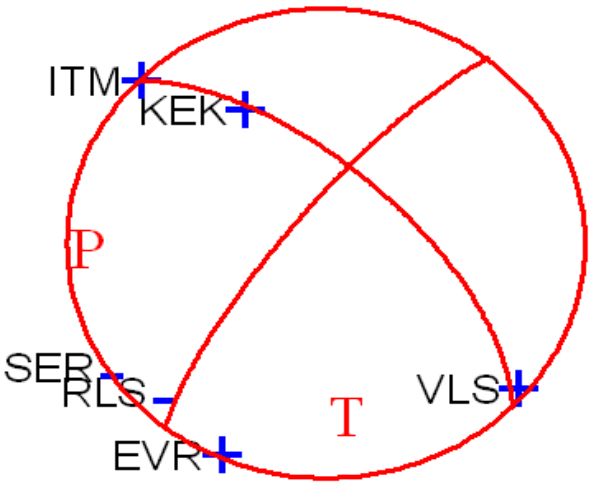

Figure 4.28: Vartholomio earthquake, red curve - mechanism from step 2 (centroid), blue signs - first-motion polarities.

4.3 Lefkada aftershock

One strong event and many moderate aftershocks occurred on the island of Lefkada, Western Greece on August 14, 2003. The sequence started by mainshock ($M_w \sim 6.2$) at 5:14:54 UTC, see Papadopoulos et al. (2003), Karakostas et al. (2004), Benetatos et al. (2005) and Zahradník et al. (2005b). Here we study the largest aftershock ($M_w \sim 5.5$) which occurred at 16:18:04 UTC. This and many other aftershocks of Lefkada were studied by Benetatos et al. (2005). The source parameters determined from five agencies are in Table 4.14.

agency	origin time (UTC)	Lat.N (deg)	Lon.E (deg)	depth (km)	M_0 (10^{17}Nm)	mag *)
SED $^+$)	16:18:2	38.826	20.573	15	2.25	5.53
MEDNET $^+$)	16:18:6.9	38.70	20.44	16	1.8	5.4
HARVARD $^+$)	16:18:7.8	38.58	20.67	15	2.01	5.5
PATNET	16:18:3.47	38.788	20.663	15.18		5.25
NOA	16:18:3.9	38.76	20.63	9		5.2

agency	strike (deg)	dip (deg)	rake (deg)	strike (deg)	dip (deg)	rake (deg)	DC%
SED	180	63	90	1	27	91	94
MEDNET	179	66	88	3	24	94	94
HARVARD	182	70	91	358	20	87	91

Table 4.14: Basic information about the largest aftershock of Lefkada from five agencies.

*) 'Mag' means magnitude, for PATNET duration magnitude, for NOA local magnitude and for the other agencies it is moment magnitude M_w.
$^+$) origin time, latitude and longitude are for centroid

We selected nine broadband stations with epicentral distance ranging from 70 to 280 km, see Table 4.15 and Figure 4.29. Locations of SED, PATNET and NOA are very near to each other; formally we choose the PATNET epicenter.

Single point solution.
We started from single point solution with all stations, and we could not fit the EVR-EW component, see Figures 4.32 and 4.34 (discussed later). Therefore we study record from this station in more detail. We integrated velocity record in the whole frequency band, used method from Chapter 3 and we removed long period disturbance - 'mouse-1' type from this record, see Figure 4.30. At the other stations and components we subtracted smaller mice (mostly 'mouse-2' type, at station SER on horizontal components it was 'mouse-1' type).

To find the centroid, we first tested 10 positions with DZ = 5 km below epicenter (PATNET) in frequency band 0.04 - 0.08 Hz. We started from the depth of 5 km, and continued from the same starting position with DZ = 2 km. From this step (step 1 from

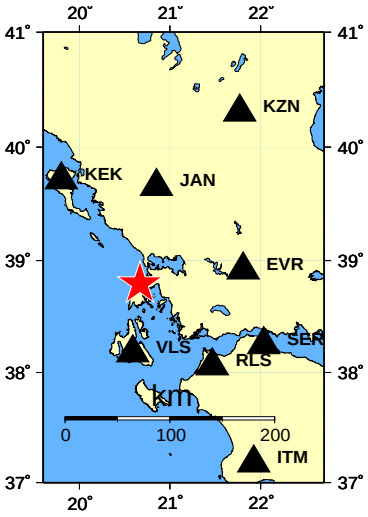

Figure 4.29: Lefkada earthquake (largest aftershock) - red star: location from PATNET, black triangles: eight from nine stations used for the Lefkada earthquake; the ATH station is outside this figure.

Chapter 2.3) we got the centroid depth = 7 km, see Figure 4.31. The maximum is sharp, so it seems that the depth is determined with pretty good resolution. But, an additional analysis reveals a more complexity. In fact, the very low correlation in the depth 5 km is caused by discontinuity in the crustal model in the same depth. After recomputing this step with the first trial position in 5.1 km (instead of 5 km) we got the correlation 57% for that position. The resulting 7 km depth is near to the estimate of Benetatos et al. (2005) (8 km) and the estimate of NOA (9 km). On the other hand, major agencies reported depths around 15 km.

The mechanisms found before and after removing these disturbances are very similar. Strike-dip-rake combination was 177, 72, 89 (358, 18, 92) before removing and 172, 73, 85 (8, 17, 105) after removing 'mouse-1' type. Scalar seismic moment was $M_0 = 1.0.10^{17}$ Nm both before and after removing. Nevertheless, after subtracting the disturbance on station EVR, we got much better fit on that station than before; see Figure 4.32.

We tested number of stations needed for inversion (mainly the case before and after removing 'mouse-1' type at station EVR, EW component). All tests were made with and without weights and in all cases the results were very similar. For all tests we believe that correct result is near the above mentioned mechanism retrieved from nine stations (i.e. also close to the result of the agencies).

- Inversion from 1 station
  For this event, inversion from one nearest station gave a wrong mechanism (from station VLS we got strike-dip-rake combination 185, 66, 102 (337, 27, 66)). Difference between this mechanism and that from nine stations is up to 20 degree. [1]

[1]For some other application (e.g. Amfilochia earthquake) we got a good solution even from one nearest station.

Station	Distance (km)	Azimuth (deg)
VLS	68.8	185.8
JAN	97.3	9.2
EVR	100.0	81.0
RLS	107.2	139.2
KEK	126.9	324.0
SER	133.5	116.5
KZN	193.0	29.0
ITM	210.3	148.0
ATH	281.4	107.9

Table 4.15: Stations used for the Lefkada aftershock

- Inversion from two near stations (in distances up to 100 km)
  The two nearest stations (VLS and JAN) appear to be most important for the inversion. Inversion from one of them, plus station EVR, gave good results even with EVR record before removing 'mouse'.

- Inversion from station EVR and one intermediate-distance station - e.g. RLS
  - before removing 'mouse' - this solution was bad: 335, 36, -101 (169, 55, -82).
  - after removing 'mouse' - we got solution near to that from nine stations.

- Inversion from three stations - EVR and two distant stations (e.g. KEK and KZN)
  - before removing 'mouse' - this solution was bad: 348, 35, -91 (170, 55, -89).
  - after removing 'mouse' - we got as good solution as from nine stations: 171, 77, 90 (351, 13, 90).

- Inversion from four stations
  In inversion from arbitrary four stations (we tested 5 combinations of stations) we got the same mechanism as from nine stations.

In step 2 (see Chapter 2.3) we fixed the 7 km depth and tested 25 positions in a horizontal (5 x 5) grid with spacing DX = DY = 2 km. Thus we got the centroid shift of 2 km to the west, see Figure 4.33.

Using a different method, that of Dreger and Helmberger (1990,1993), Benetatos et al. (2005) obtained the very similar focal mechanism; their strike-dip-rake combination was 179, 67, 95 (345, 23, 77). However, there is an important difference between our solution and that of Benetatos et al. (2005). They presented seismograms at only 4 stations (VLS, RLS, KEK and ATH), while we fitted five on NS component, nine on EW component and eight on Z component.

Generally they have problem with larger events. For smaller events (M $\sim$ 3.5-4.5) they fit roughly 7 stations. For magnitude 5 they explain only 2-4 stations. Their frequency band was very similar 0.05-0.08 Hz (our was 0.04-0.08 Hz). Difference between our and

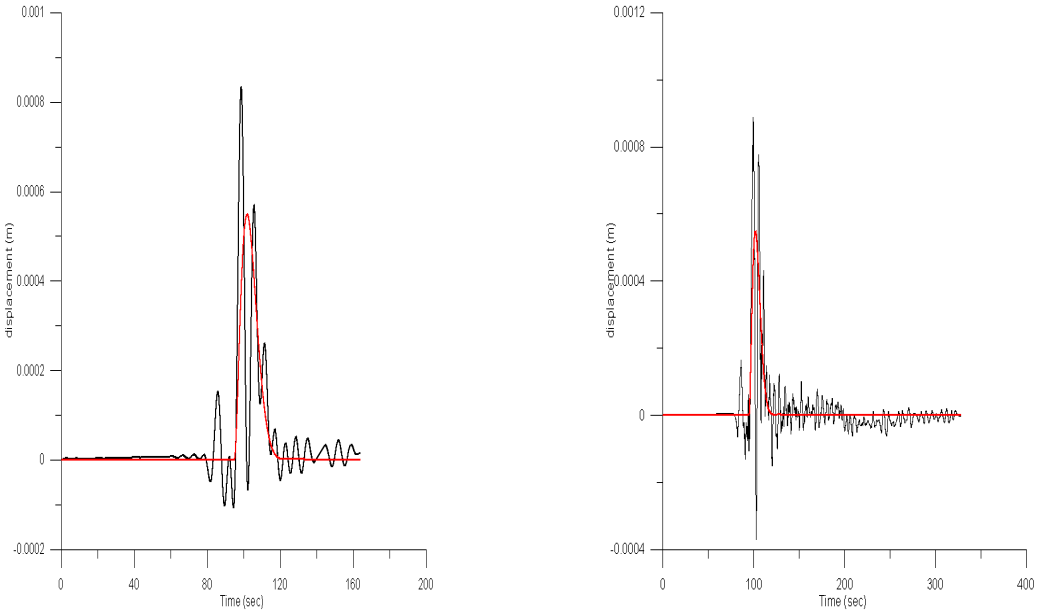

Figure 4.30: Mouse on station EVR, left panel: black curve - integrated filtered (0.-0.-0.15-0.2) velocity record, red curve - model response of step in acceleration with amplitude A=1.4e-4 m/s^2, right panel: black curve - integrated unfiltered velocity record, red curve - same as left panel

their solution can have many reasons: different method, crustal model, 'mice' (especially at station EVR), etc.

Multiple point solution

In step 3 we tested 25 trial positions in both nodal planes passing through the centroid. From empirical relations we got rupture area A = 35 km^2 and area covered by asperities A_a = 8 km^2. Therefore, assuming that the asperity size may be of the order of 3 x 3 km, we extended the frequency band (0.02-0.04-0.3-0.32 Hz) and used the spacing DS = DD = 2 km. As result for nodal plane II (strike = 8) we got mechanism 178, 77, 87 (11, 13 103), scalar moment for this subevent was $M_0 = 9.68.10^{16}$ Nm. For both nodal planes we got better fit of seismograms with only 1 subevent at EW and Z component, see Figure 4.35. The NS component has the least amplitude and it was not successfully explained even at the low-frequency point solution. That is why we cannot expect good fit on NS for multiple point solution at higher frequencies. We interpret this result as indication that the studied aftershock was a relatively simple event, not a multiple event.

Polarity

We compared the centroid focal mechanism from step 2 with the first-motion polarities. Some of our stations are located near one nodal plane of solution from step 2. Correspondingly, at these stations, polarity is very unclear. In Figure 4.37 we label them with question mark. As a result, our mechanism agrees with the first-motion polarities. It means that there was no significantly different rupture style between the nucleation stage and the "average" whole-fault process.

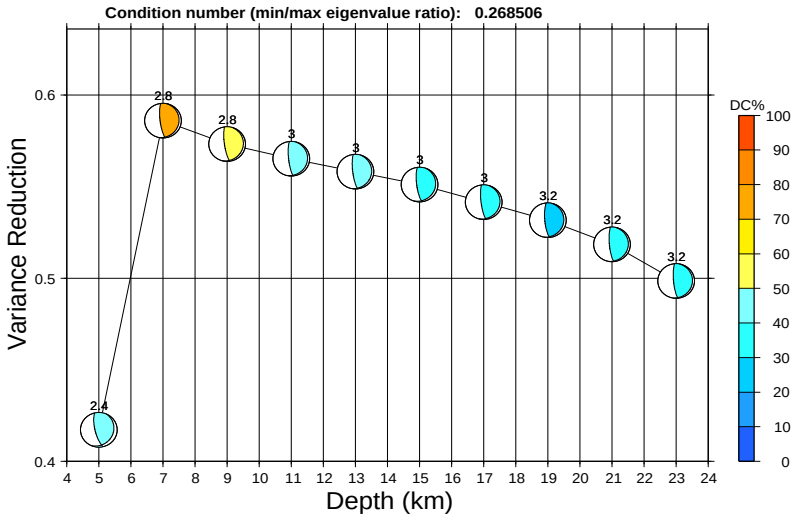

Figure 4.31: Lefkada aftershock, variance reduction as a function of the depth with mechanism for each position. Colors represent the DC percentage. Numbers above beach balls express optimal time shifts.

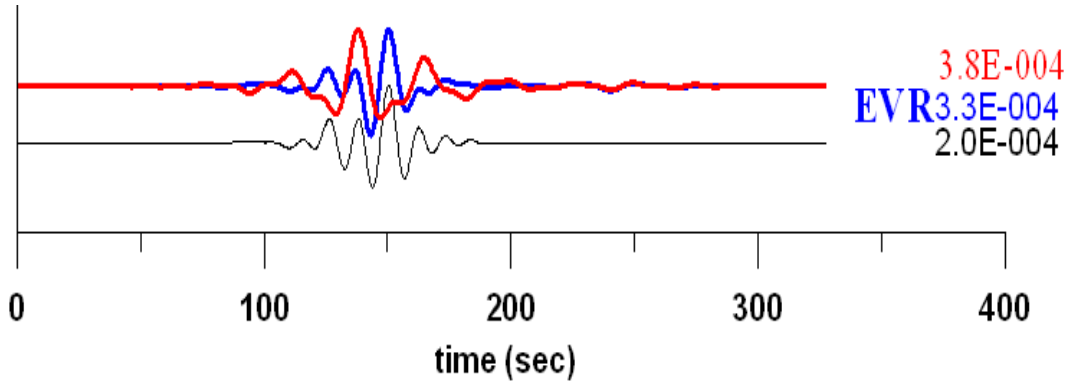

Figure 4.32: Lefkada aftershock. Top red curve - observed displacement without removing 'mouse', top blue curve - observed displacement with removing 'mouse', bottom black curve - synthetic displacement, f = 0.04-0.08 Hz.

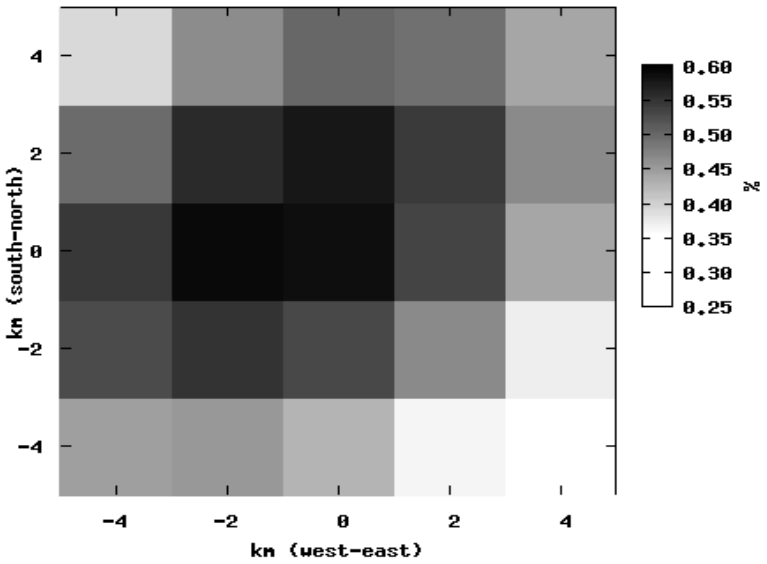

Figure 4.33: Lefkada aftershock, maximum correlation for each trial source position. In center of the plane is the epicenter (PATNET).

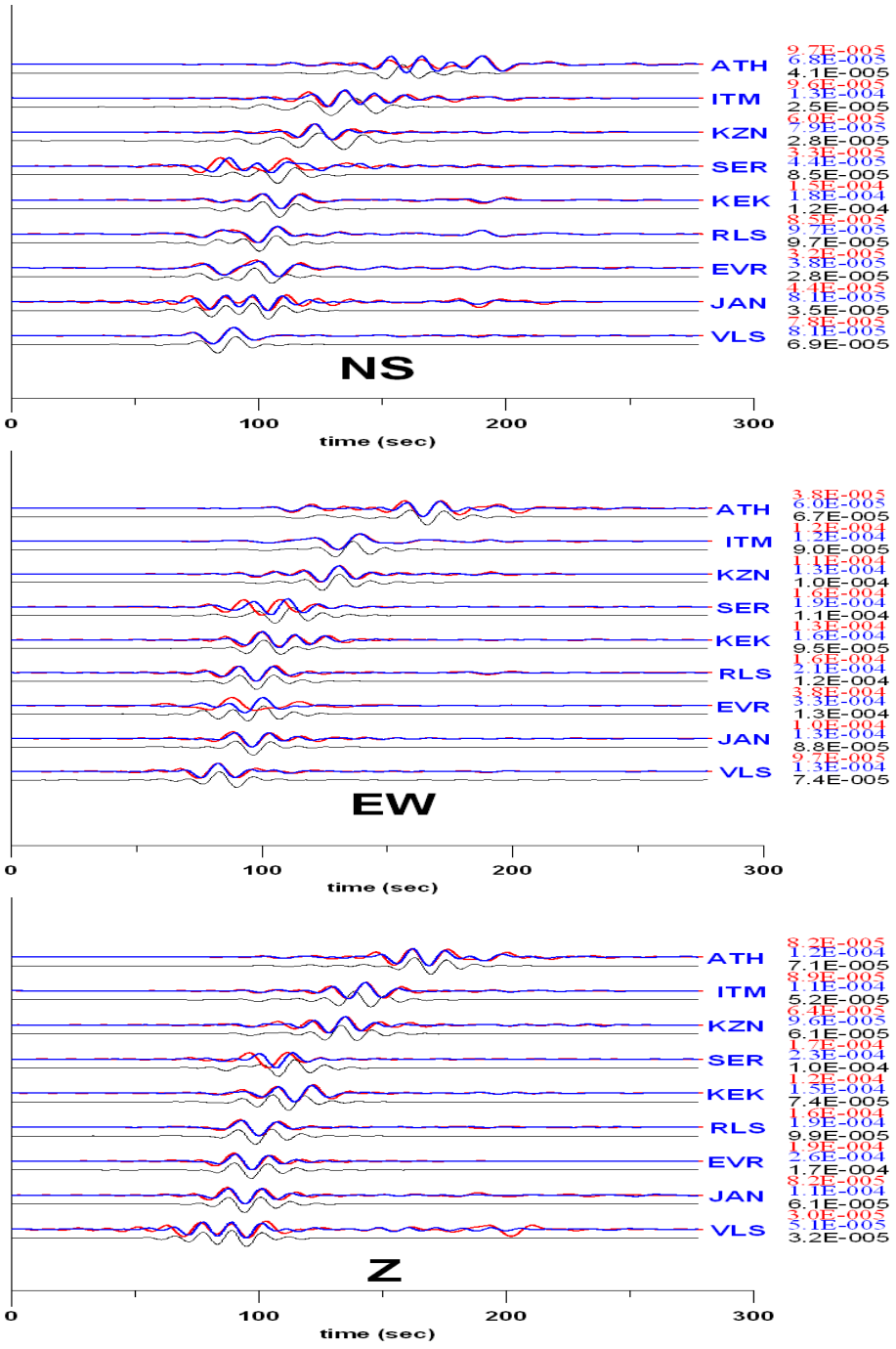

Figure 4.34: Lefkada aftershock. Point source solution, f = 0.04-0.08 Hz, top (red) curves - observed displacement without removing 'mice'. Top (blue) curves - observed displacement with removing 'mice', bottom (black) curves - synthetic displacement from step 1.

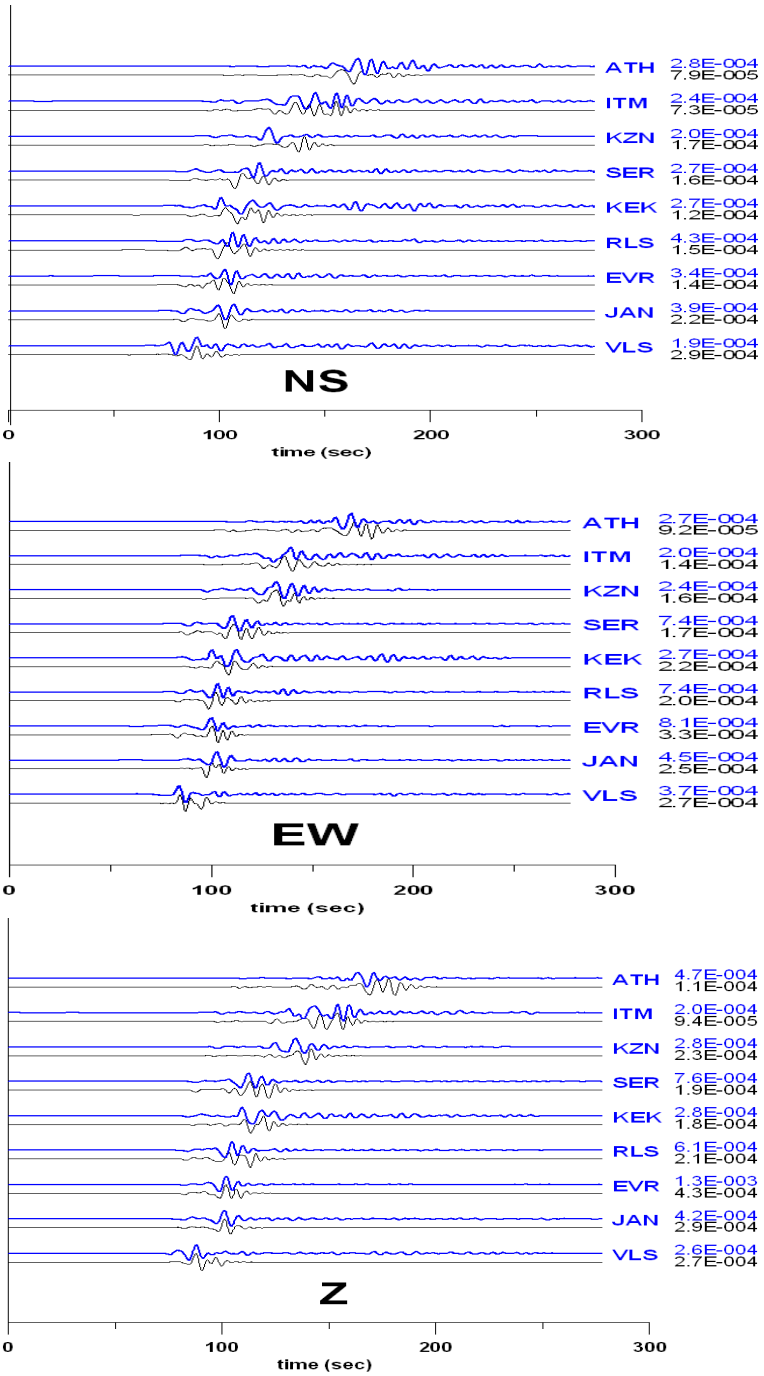

Figure 4.35: Lefkada aftershock, multiple point solution, top blue curves - observed displacement, black curves - synthetic seismograms for 1 subevent, f = 0.04-0.3 Hz.

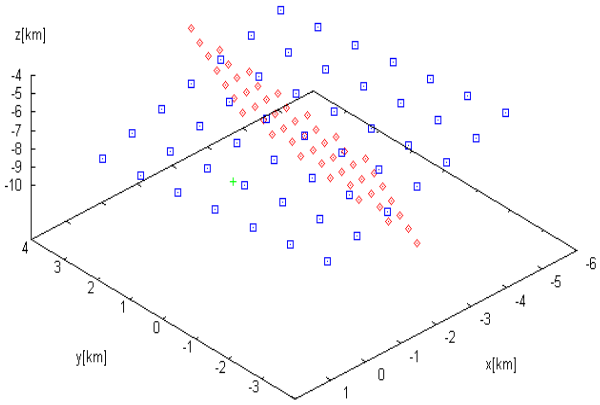

Figure 4.36: Lefkada earthquake, red points - nodal plane I, blue points - nodal plane II, green point - hypocenter. Both nodal planes are passing through centroid from step 2. Size of both plane is 6 x 6 km, with DS = DD = 1 km.

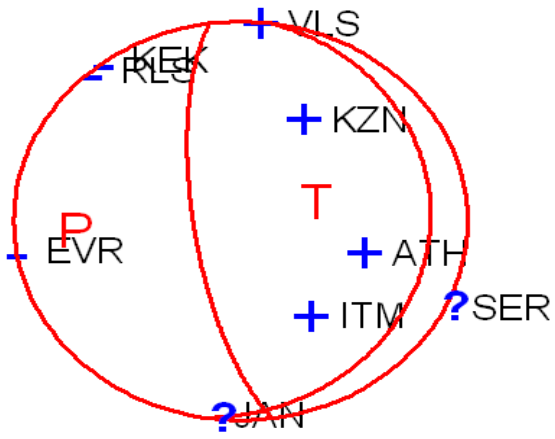

Figure 4.37: Lefkada aftershock, red curve - focal mechanism from step 2, blue signs - first motion polarity.

uncertain polarities are label with question mark

Chapter 5

Discussion and conclusion

In this thesis we studied three earthquakes located in western Greece. We used and tested possibilities of the ISOLA method. This method computes the multiple point solution (subevents). For each earthquake we discuss physical justification of each subevent. Before using ISOLA method we prepare data for inversion in a series of operations (integration, filtration, instrumental correction, etc.). During this processing stage we detected and removed some long-period disturbances. Newly in this thesis, a 'mouse-2' type disturbance was detected, modeled and removed from signal.

We studied three events from different regions in western Greece. For all of them, we used the crustal model of Haslinger et al. (1999). This model was deduced for region near Amfilochia earthquake, and we think that this is a reason (one of several reasons) why we got the best results just for that event. Besides specific results for the individual events (summarized in the preceding chapters), several general conclusions can be drawn.

- Selective sensitivity
  For all studied events we found a very selective sensitivity of stations with respect to focal mechanism. Significant changes in mechanism (e.g. 20 to 30 degrees in strike, dip and rake compared to a reference solution from major agencies) evoke typically a significant change of waveforms at only one component at one station (or, 2 to 3 components as a maximum from 15 to 20 studied components). These sensitive components have big importance for inversion. They should have large weights in future applications. Another example is shown in Figure 4.4.

- Resolution in dip direction
  For all applications we got much better resolution of subevent position in strike direction than in dip direction on the fault planes.

- Seismic moment: point x multiple point solution
  If we accept some criteria for significant subevents and then we find that the summary moment for one or more subevents (two for Amfilochia, three for Vartholomio and one for Lefkada aftershock) is the same as that we got from point solution, it serves as a posterior check of number of subevents.

- ISOLA in automated solution
  It is hard (if not impossible) to use ISOLA for automated inversion. Long-period disturbances should be detect and removed. Moreover, very often there can be two maxima in the correlation diagram with nearly equal amplitudes, a "correct" and a "bad" one (their only difference is in rake or rake + 180 degrees). The other problems include, for example, a very low resolution in some cases and then it is quite wrong if the user formally selects position and timing of subevents based solely on the formal correlation maximum. Number of subevents that we can trust needs always a detailed analysis (see Chapter 4.1 - Amfilochia).

Main conclusion is that this method can provide basic information about centroid and major asperities on the fault. We can determine fault plane from mutual position of centroid and hypocenter. Important observation is that quality of the solution for the three studied events is difficult. Reasons are not quite clear. They may include both physical factors (size of earthquake, complexity of the source process, crustal model) and formal factors (frequency range, gridding of the fault plane). More studies are needed to clarify these issues and to formulate criteria how to better use and improve the method. As a continuation we work also on Cythera M6.2 earthquake from January 8, 2006 and several Zakynthos M5.5 events from April, 2006.

Appendix A

Shortcuts

NOA	National Observatory of Athens
SED	Schweizerischer Erdbebendienst
MEDNET	Mediterranean Very Broadband Seismographic Network
PATNET	The Patras Seismological Lab Radiolink Seismic Network
USGS	US Geological Survey
WILBER II	Web Interface to Lookup Big Events for Retrivel
ORFEUS	Observatories and Research Facilities for EUropean Seismology
SAC	Seismic Analysis Code
SEED	Standard for the Exchange of Earthquake Data
UTC	Universal Time, Coordinated
EMSC	European-Mediterranean Seismological Centre

References

Benetatos, Ch., A. Kiratzi, Z. Roumelioti, G. Stavrakakis, G. Drakatos, and I. Latoussakis (2005). The 14 August 2003 Lefkada Island (Greece) earthquake: Focal mechanisms of the mainshock and of the aftershock sequence, Journal of Seismology, **9**, 2, 171-190.

Bouchon, M. (1981). A simple method to calculate Green's functions for elastic layered media, Bull. Seis. Soc. Am. **71**, 959-971.

Dreger, D., and D. Helmberger (1990). Broadband modelling of local earthquakes, Bull. Seis. Soc. Am., **80**, 1162-1179.

Dreger, D., and D. Helmberger (1993). Determination of source parameters at regional distances with single station or sparse network data, J. Geophys. Res. **98**, 8107-8125.

Haslinger, F., E. Kissling, J. Ansorge, D. Hatzfeld, E. Papadimitriou, V. Karakostas, K. Makropulos, H.-G. Kahle, and Y. Peter (1999). 3D crustal structure from local earthquake tomography around the Gulf of Arta (Ionian region, NW Greece), Tectonophysics **304**, 201-218.

Karakostas, V.G., E.E. Papadimitriou, and C.B. Papazachos (2004). Properties of the 2003 Lefkada, Ionian Islands, Greece, Earthquake Seismic Sequence and Seismicity Triggering, Bull. Seis. Soc. Am. **94**, 5, 1976-1981.

Kikuchi, M., and H. Kanamori (1991). Inversion of complex body waves-III, Bull. Seis. Soc. Am. **81**, 6, 2335-2350.

Papadopoulos, G.A., V.K. Karastathis, A. Ganas, S. Pavlides, A. Fokaefs, and K. Orfanogiannaki (2003). The Lefkada, Ionian Sea (Greece), shock (Mw 6.2) of 14 August 2003: Evidence for the characteristic earthquake from seismicity and ground failures, Earth Planets Space **55**, 713-718.

Plešinger, A., P. Jedlička, J. Soukup (2002). Spurious long-period components in broadband records of high-frequency ground motions: observation, computer simulation, shock table experiments (unpublished report), Geophysical Institute of the Academy of Sciences of the Czech Republic.

Roumelioti, Z., Ch. Benetatos, A. Kiratzi, G. Stavrakakis, and N. Melis (2004). A study of the 2 December 2002 (M5.5) Vartholomio (western Peloponnese, Greece) earthquake and its largest aftershocks, Tectonophysics **387**, 65-79.

Somerville, P., K. Irikura, R. Graves, S. Sawada, D. Wald, N. Abrahamson, Y. Iwasaki, T. Kagawa, N. Smith, and A. Kowada (1999). Characterizing crustal eartquake slip models for prediction of strong ground motion, Seimol. Res. Letters **70**, 59-80.

Wessel, P., W.H.F. Smith (1991). Free Software Helps Map and Display Data. EOS Trans. AGU **72**, 441, 445-446.

Zahradník, J., and E. Sokos (2004). Problematic non-shear mechanism of moderate earthquakes in western Greece, European Seismological Commission XXIX General Asembly (Abstracts), 107.

Zahradník, J., and A. Plešinger (2005a). Long-period pulses in broadband records of near earthquake, Bull. Seis. Soc. Am. **95**, 1928-1939.

Zahradník, J., and A. Serpetsidaki, E. Sokos, G-A. Tselentis (2005b). Iterative Deconvolution of Regional Waveforms and a Double-Event Interpretation of the 2003 Lefkada Earthquake, Greece, Bull. Seis. Soc. Am. **95**, 1, 159-172.